

UNIVERSITÀ DEGLI STUDI DI NAPOLI FEDERICO II



SCUOLA POLITECNICA E DELLE SCIENZE DI BASE

Dipartimento di Ingegneria Chimica, dei Materiali e della
Produzione Industriale

Classe delle Lauree Magistrali in Ingegneria Chimica
Classe LM-22

TESI DI LAUREA MAGISTRALE IN INGEGNERIA CHIMICA

**Numerical simulations of droplet dynamics through an
orifice - pin system for pyroelectrodynamic shooting**

**Simulazioni numeriche della dinamica di una goccia
attraverso un sistema orifizio - pin per lo shooting
piroelettrodinamico**

Supervisor
D'Avino Gaetano

Candidate
Pentella Domenico
Matr. M55000852

ACADEMIC YEAR 2019 -2020

Contents

ABSTRACT	6
1 INTRODUCTION	7
1.1 Microfluidics	8
1.2 High resolution Printing	12
1.2.1 Pyro-Electrohydrodynamic Dispenser	13
1.2.2 Pyro-Electrohydrodynamic improvement.....	16
1.2.3 Liquid nanoprinting and patterning	19
1.3 Dynamics in microfluidic systems	22
1.3.1 Characteristic dimensionless numbers	23
1.3.2 Characteristic times	25
1.3.3 Droplet and surface properties in droplet dynamics through an orifice	26
1.4 Previous study	29
1.5 Aim of the work	32
2 THE METHOD	33
2.1 Geometry	33
2.2 Mathematical model	35

2.3 Numerical discretization	39
2.3.1 Volume discretization	40
2.3.2 Time stepping and computational time	42
2.4 SensApp set up	42
2.4.1 Heat transfer devices	43
3 NUMERICAL SIMULATIONS OF DROPLET DYNAMICS THROUGH AN ORIFICE-PIN SYSTEM	46
3.1 Simulations of distilled water droplet through an orifice-pin system	46
3.1.1 Simulations on CNR's standard geometry	47
3.1.2 Simulations with $D_2 = 0.8$ mm	51
3.1.3 Simulations with $D_2 = 0.5$ mm	55
3.2 Simulations of different fluids droplet through an orifice-pin system	59
3.2.1 Simulations with variable Ca and Bo by variation of surface tension at fixed $Re = 1.928$	60
3.2.2 Simulations with variable Ca and Re by variation of kinematic viscosity at fixed $Bo = 0.5209$	66

3.2.3 Other Simulations varying Bo , Re and Ca simultaneously	67
3.3 Meniscus formation and complete dynamic	71
3.4 Effect of initial velocity	75
4 CONCLUSIONS	77
BIBLIOGRAPHY	79

ABSTRACT

Questo lavoro di tesi nasce dalla collaborazione dell'Università di Napoli Federico II e l'Istituto di Scienze Applicate e Sistemi Intelligenti del Consiglio Nazionale delle Ricerche (CNR-ISASI) per il progetto Europeo Comunitario **SensApp**, finanziato dall'European Union's Horizon 2020 research and innovation programme (Sovvenzionamento No 829104). Il progetto coinvolge anche altri partner, tra i quali: Vrije Universiteit Brussel VUB, Johannes Kepler University Linz JKU, Technical Research Centre of Finland VTT, Centro Neurolesi Pulejo Messina e Ginolis GIN. La finalità del progetto SensApp è lo sviluppo di un super-sensore per la diagnosi precoce dell'Alzheimer tramite prelievo di sangue, in particolare, in questa tesi, si eseguono delle simulazioni numeriche per modellare la dinamica di una goccia all'interno di un sistema orifizio-pin. Le simulazioni numeriche sono effettuate mediante un codice basato sul metodo dei volumi finiti (VOF) per fluidi Newtoniani e sono effettuate al variare di angoli di contatto, raggio della goccia, superficie di passaggio, viscosità cinematica, tensione superficiale e densità del liquido.

CHAPTER 1

INTRODUCTION

The Alzheimer's disease (AD) is a progressive and irreversible neurodegenerative disorder, which leads to death. It represents the major cause of dementia in the elderly population, with a great socio-economic impact in the worldwide community. Estimates vary, but experts evaluated that nowadays around 30 million of people are affected by AD and, taking into account the increase of life expectation, this community is likely to rise to about 150 million people by 2050. The current guidelines for clinical diagnosis of AD establish the determination of specific protein biomarkers (Amyloid-beta, tau, P-tau) in cerebrospinal fluid (CSF) through ELISA kit and positron emission tomography (PET) of the brain with amyloid tracer. However, PET is highly expensive and not always available in clinics and lumbar puncture for CSF collection is an extreme invasive intervention that requires hospitalization and hinders follow-up programs during therapies. Nowadays the traditional ELISA¹ kits cannot determine such biomarkers in peripheral blood due to their abundance well below the standard sensitivity that is of 50-100 pg/mL. Therefore, by the time it is recognized, the disease has been progressing for many years. In this framework an early diagnosis of AD is crucial for saving lives.

SensApp aims at developing a super-sensor system that, pushing the sensitivity well below 1 pg/mL, will be able to detect the AD biomarkers (Amyloid-beta, tau, P-tau) in human plasma, thus overcoming the limits of detection usually encountered by standard ELISA protocols. This super-sensor will enable in future a faster and non-invasive early diagnosis of AD simply through a routine blood test, thus opening the route to highly efficient screening programs among the population².

Researchers are focusing on manipulating and dispensing tiny droplets in nanotechnology and biotechnology in order to push sensitivity below current standards in most areas possible.

So, microfluidic systems have been thought to create a new experimental format for processing ultra-small analytic volumes with high efficiency.

1.1 Microfluidics

Microfluidics is the science and technology of systems that process and manipulate small amounts of liquids (from 10^{-9} to 10^{-18} litres) using channels of tens or hundreds of micrometres in size³.

Major advantages of a microfluidic approach are faster transport dynamics, lower consumption of fluid, lower manufacturing costs and compactness of the system.

The behaviour of fluids at the microscale can differ from macrofluidic behaviour because some factor such as surface tension, energy dissipation, and fluidic resistance start to interact more with the system. Various kinds of microfluidic flows have been analysed and each of these flows need a specific technique to maintain its characteristic. The main ones are Open Microfluidics, Continuous-flow Microfluidics, Droplet-based Microfluidics, Digital Microfluidics, Paper-based Microfluidics, Particle Detection Microfluidics and Microfluidic-Assisted Magnetophoresis.

In Open Microfluidics at least one boundary of the system is removed, exposing the fluid to air or another interface (Fig.1.1).

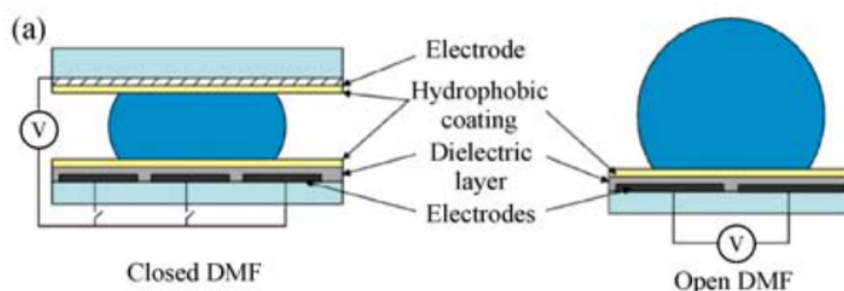


Fig.1.1: Side-view schematics of the parallel-plate (left) and single-plate (right) DMF devices (Wang, H., Chen, L. & Sun, L. Digital microfluidics: A promising technique for biochemical applications. *Front. Mech. Eng.* 12, 510-525 [2017]).

Continuous flow microfluidics rely on the control of a steady state liquid flow through narrow channels or porous media predominantly by accelerating or hindering fluid flow in capillary elements⁴.

Droplet-based microfluidics is a subcategory of microfluidics in contrast with continuous microfluidics; droplet-based microfluidics manipulates discrete volumes of fluids in immiscible phases with low Reynolds number and laminar flow regimes. Interest in droplet-based microfluidics systems has been growing substantially in past decades. Microdroplets allow for handling miniature volumes (μl to fl) of fluids conveniently, provide better mixing, encapsulation, sorting, and sensing, and suit high throughput experiments⁵.

Alternatives to the above closed-channel continuous-flow systems include novel open structures, where discrete, independently controllable droplets are manipulated on a substrate using electrowetting. Following the analogy of digital microelectronics, this approach is referred to as digital microfluidics (DMF)⁶.

Paper based microfluidics rely on the phenomenon of capillary penetration in porous media. To tune fluid penetration in porous substrates such as paper in two and three dimensions, the pore structure, wettability and geometry of the microfluidic devices can be controlled while the viscosity and evaporation rate of the liquid play a further significant role⁷.

Particle detection of small fluid-borne particles down to about $1\ \mu\text{m}$ in diameter is typically done using a Coulter Counter, in which electrical signals are generated when a weakly-conducting fluid such as in saline water is passed through a small ($\sim 100\ \mu\text{m}$ diameter) pore, so that an electrical signal is generated that is directly proportional to the ratio of the particle volume to the pore volume.

Recent developments in the microfluidics field have seen the integration of microfluidic devices with magnetophoresis: the migration of particles by a magnetic field. This can be accomplished by sending a fluid containing at least one magnetic component through a microfluidic

channel that has a magnet positioned along the length of the channel. This creates a magnetic field inside the microfluidic channel which draws magnetically active substances towards it, effectively separating the magnetic and non-magnetic components of the fluid⁸.

Among all these particular flows, Digital Microfluidics (DMF) includes all the advantages of conventional microfluidics and offers more, such as: precise control over unit droplets, easy integration with measurement techniques, multiplex assay capability and there is no need for propulsion devices. A DMF device set-up depends on the substrates used, the electrodes, dielectric material, the thickness of that dielectric material, the hydrophobic layers, and the applied voltage⁹. In the parallel-plate format, droplets are sandwiched between two parallel plates wherein electrodes are patterned. The lower plate consists of an array of actuation electrodes, whereas the upper plate serves as the ground electrode consisting of a transparent conductive material (e.g., indium tin oxide (ITO)). Electrodes are covered with a layer of dielectric material to restrict the electric current and prevent electrolysis and a hydrophobic coating is also deposited on top of the insulating layer, which is mainly to increase the contact angle and reduce contact angle hysteresis. The droplets in many DMF devices are manipulated in the air, although other filler media (e.g., silicone oil) can lower the evaporation rate and decrease the voltage required to actuate the droplets. When applying a series of electrical potentials to an array of actuation electrodes in DMF devices, each droplet is controlled independently to perform corresponding operations because the droplet wettability on a solid surface is electrically changed to produce a motion, and this is caused by the electrical force concentrating on the triple-phase contact line. The concentrated electrical force results in a change in the contact angle, which in turn, leads to a capillary pressure that causes the droplet movement¹⁰ (Fig.1.2).

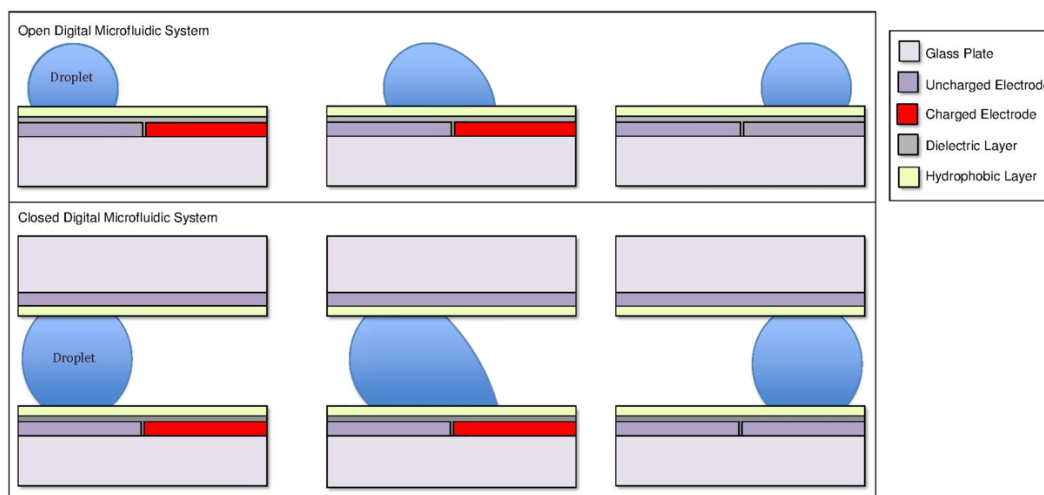


Fig.1.2: A droplet being transported in a one- and two-plate DMF device. The passage of time is shown left to right. The droplet moves onto the adjacent charged electrode (https://commons.wikimedia.org/wiki/File:DMF_open_and_closed_system.pdf).

Based on this particular application of electrostatic fields, different dispensing methods have been studied, such as the electrohydrodynamic jetting, which involves a tube with a meniscus bearing a Taylor cone profile spraying a fine jet, the pulsed electrohydrodynamic liquid jetting to obtain droplets on demand with sizes much smaller than the original ones, microcapillary nozzles to have high resolution electrohydrodynamic jet printing or drop-on-demand printing of conductive ink. For example, in the electrohydrodynamic jetting there are two layers in the nozzles including the nozzle layer, the reservoir layer and electrodes are deposited to realize the electric connection in the nozzle layer. The inside flow channels ensure the solution supply to nozzle orifices. The electric field leads to accumulation of the mobile ions in the liquid and the electrostatic interaction between ions creates the conical shape of the meniscus called “Taylor cone”. The droplets eject from the cone when the electrostatic stresses overcome the surface tension (Fig.1.3)

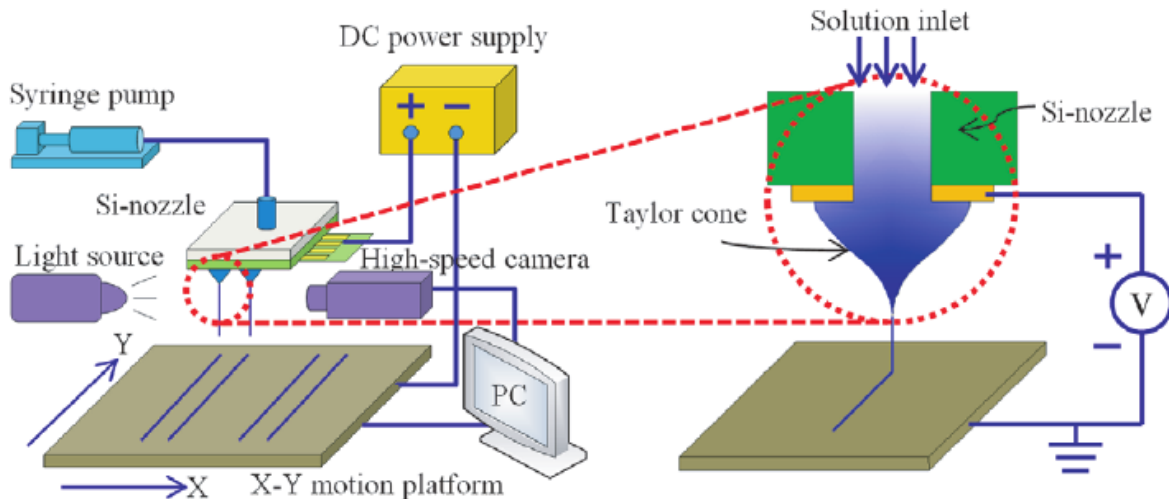


Fig.1.3: Taylor cone formation. Patterned gold electrodes deposited to realize the electric connection in the nozzle layer. The patterned gold electrodes with orifices are fabricated through Si-based micromechanical machining processes. The reservoir layer is made of PDMS using a mould forming process (Yanqiao Pan *et al* 2013 *J. Phys. D: Appl. Phys.* **46** 255301).

1.2 High Resolution Printing

Techniques for liquid dispensing and patterning with inorganic, organic and biological inks at high resolution represent one of the major points of interest in different fields of technology from experimental to industrial applications. Different printing methods have been developed in recent years: stationary liquid microjets dispense droplets by inducing fluid interface instabilities¹¹, whereas atomic force microscope probes dispense nanolitre droplets through an aperture in their apex. Other approaches make use of electrohydrodynamic (EHD) jetting, which involves a tube with a meniscus bearing a Taylor cone profile spraying a fine jet. In fact, it is also possible to use electric fields to draw narrow jets of liquids from fine apertures¹². Using pens based on micro or nanoscale glass capillaries, the EHD effects enable printing with resolution approaching 100 nm using pigments and a variety of advanced materials (conducting polymers, carbon nanotubes, oligonucleotides and colloids). On-demand droplets with smaller sizes

than that of the delivery nozzle can be obtained by pulsed EHD liquid jetting or through the application of electrostatic fields. The EHD techniques provide sub-micrometre droplets and have the flexibility to pattern fragile organics and biological materials that are, instead, incompatible with conventional methods such as photolithography. However, dispensing this kind of liquids requires the arrangement of appropriate electrodes and the use of high-voltage circuits between the liquid reservoir and the receiver substrate.

A new concept of droplet generation based on the pyro-electrohydrodynamic effect has been developed for the direct drawing and dispensing of small droplets from liquid drops or film reservoirs.

1.2.1 Pyro-Electrohydrodynamic Dispenser

In the Pyro-Electrohydrodynamic dispenser the electric fields are generated pyroelectrically using functionalized substrates of Lithium Niobate (LN) for transferring liquids between two substrates and manipulate the droplets three dimensionally. When the niobate substrate is placed near a second substrate that supports ink droplets or films of liquid, the pyroelectric effect in the LN substrate can initiate electrohydrodynamic responses. So that, when the electric fields exceed a critical magnitude, pulsating jets emerge, pulling the liquid in the form of a rapid succession of fine droplets. These pulsations continue until the fields dissipate on cooling of the pyroelectric material, and the ejection of the droplets can therefore be reversibly turned on and off in this manner. The heating creates a sort of 'virtual nozzle' through localized EHD effects, thereby omitting the need for actual nozzles. So, this technique does not require electrodes, high-voltage circuit connections or special capillary nozzles. Electric forces are activated pyroelectrically by scanning a heated-tip or non-contact infrared beam on a functionalized substrate and the pyroelectric functionality of a LN substrate has been used for non-contact manipulation of liquids leading to the formation of a smart dispenser (Fig.1.4).

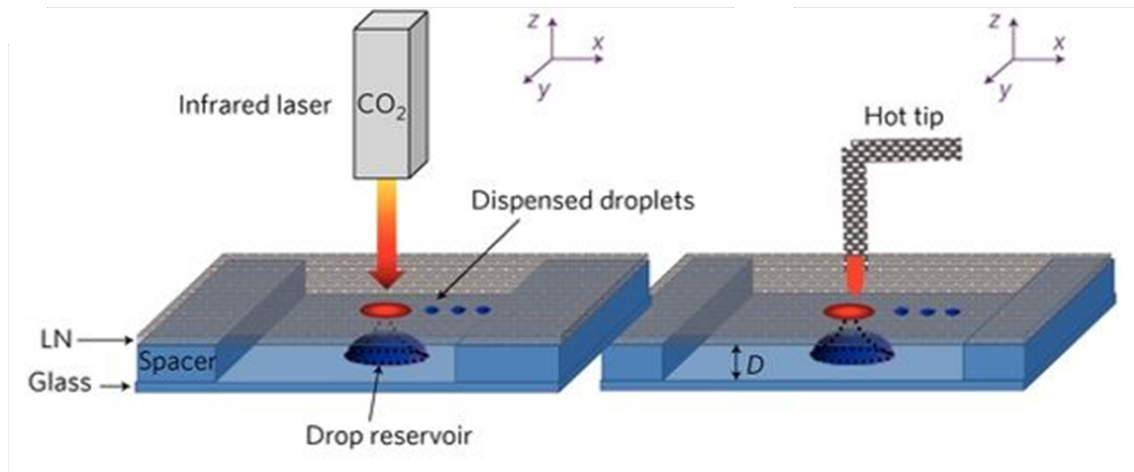


Fig.1.4: Schematic of the microfluidic system consisting of two plates and a heat source such as an IR laser (a) or hot tip (b) of a conventional soldering iron (Ferraro, P., Coppola, S., Grilli, S. *et al.* Dispensing nano-pico droplets and liquid patterning by pyroelectrodynamically shooting. *Nature Nanotech* 5, 429-435 [2010]).

The system consists of two plates and a heat source. The heat source could be a non-contact infrared beam (continuous-wave CO₂ laser emitting at 10.6 μm) or a hot tip of a conventional soldering iron, acting as a contact stimulus. A microscope glass slide forms the base of the liquid reservoir (which could be a drop or a film), and the LN crystal wafer (z-cut, optically polished and 500 μm thick) acts as an auxiliary plate that drives the process and acts as a substrate for the dispensed liquids (see Methods for more details). A pointwise thermal stimulus is applied to the LN crystal to induce the pyroelectric effect locally. The maximum operation temperature of the hot tip is ~250 °C. At equilibrium, the spontaneous polarization P_s of the LN crystal is fully compensated by the external screening charge, and no electric field exists. According to the pyroelectric effect, the temperature change ΔT causes a variation ΔP_s , which builds up an electric potential across the z surfaces (Fig1.6). Neglecting the losses, a surface charge density $\sigma = 1/4 P_c \Delta T$ appears locally when the tip heats the crystal.

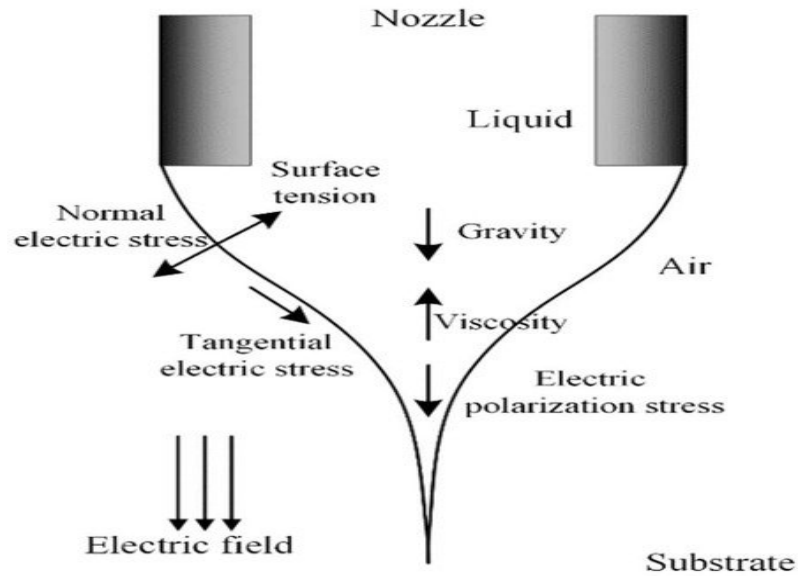


Fig.1.6: Representation of Taylor cone formation in Pyro-EHD dispenser after heat source stimulus (Pan, Y.; Zeng, L. Simulation and Validation of Droplet Generation Process for Revealing Three Design Constraints in Electrohydrodynamic Jet Printing. *Micromachines* 2019, 10, 94).

When the liquid starts to deform under the action of the electric field, two evolutions are possible in function of the critical parameter D_c . For a fixed drop volume, a critical value D_c can be defined for the distance D between the base and the substrate, according to the following expression¹⁴:

$$D_c = (1 + \theta/4)V^{1/3}$$

Where θ is the contact angle and V is the volume of the drop reservoir. A stable liquid bridge establishes when $D < D_c$ (Fig.1.7a). The most relevant case here refers to $D > D_c$, when a stable liquid bridge cannot be established between the plates, and a liquid streaming regime occurs (Fig.1.7b, c).

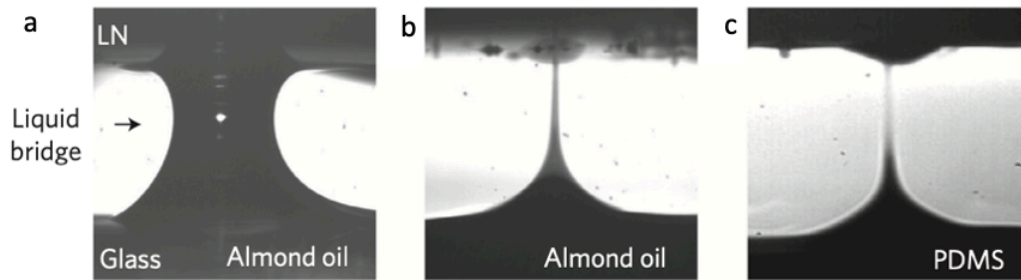


Fig.1.7: (a) Liquid bridge obtained when D is shorter than the critical distance; equation (1). (b), (c), Shooting of almond oil and PDMS, PDMS has a continuous blasting cone due to its higher viscosity (Ferraro, P., Coppola, S., Grilli, S. *et al.* Dispensing nano-pico droplets and liquid patterning by pyroelectrodynamic shooting. *Nature Nanotech* 5, 429-435 [2010]).

We use such instability to break up the liquid reservoir and to dispense droplets. Figure 1.8a, b shows two sequences of liquid shooting in which nanolitre and picolitre almond oil droplets were dispensed from a liquid film and from a sessile drop reservoir stimulated by the hot tip and by infrared laser pulses (power, 10 W; length, 100 ms), respectively.

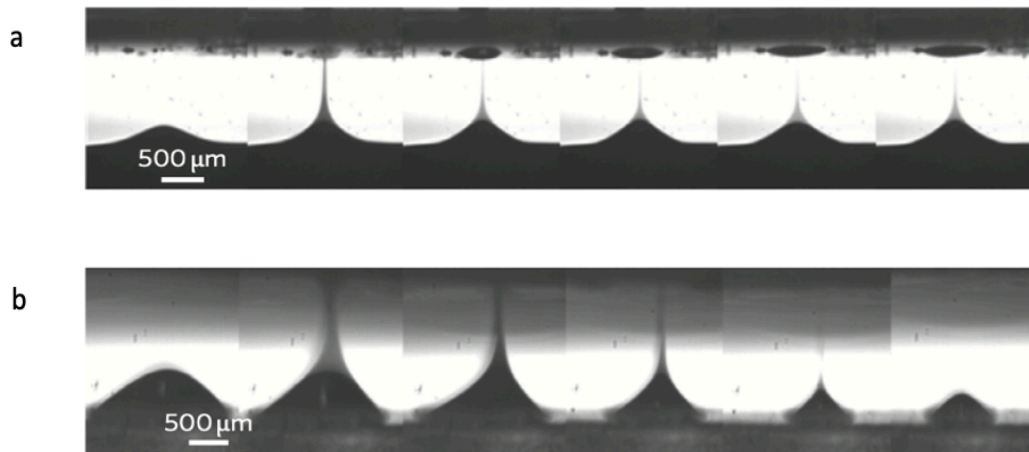


Fig.1.8: (g, h), Sequence of almond oil shots taken from a film stimulated by hot tip (g) and from a sessile drop stimulated by IR laser (Ferraro, P., Coppola, S., Grilli, S. *et al.* Dispensing nano-pico droplets and liquid patterning by pyroelectrodynamic shooting. *Nature Nanotech* 5, 429-435 [2010]).

1.2.2 Pyro-Electrohydrodynamic improvement

The pyro-electrohydrodynamic ‘dispensing gun’ may operate with various functionalities. The shooting direction can be changed within a wide solid angle (Fig.1.9a) by moving the thermal source (hot tip or laser beam). In fact, the regions with highest electric fields follow the thermal source

displacement. The off-axis shooting angles reach values up to $\sim 20^\circ$, allowing the dispenser to deposit liquids onto an area of $\sim 23 \text{ mm}^2$ from a standing drop reservoir. Larger angles induce the drop reservoir to translate during shooting and dispense to different locations (drop in Fig.1.9b and film in Fig.1.9c). The drop reservoir moves only beyond a certain threshold angle. In fact, when the drop undergoes the maximum asymmetrical deformation under the off-axis electric force, the solid-liquid surface tensions are no longer balanced and a resulting force moves the drop (Fig.1.9b). Such imbalance of surface tensions is similar to that induced by a thermal gradient in thermocapillarity. The dispensing gun moves more easily in the case of the film reservoir (Fig. 1.9c), because no solid-liquid interface tension prevents movement of the blasting cone. The sequence of images in Fig. 1.9c shows the translation of the dispensing gun up to 1.6 mm (x-axis) and 1 mm (y-axis) during shooting¹⁵.

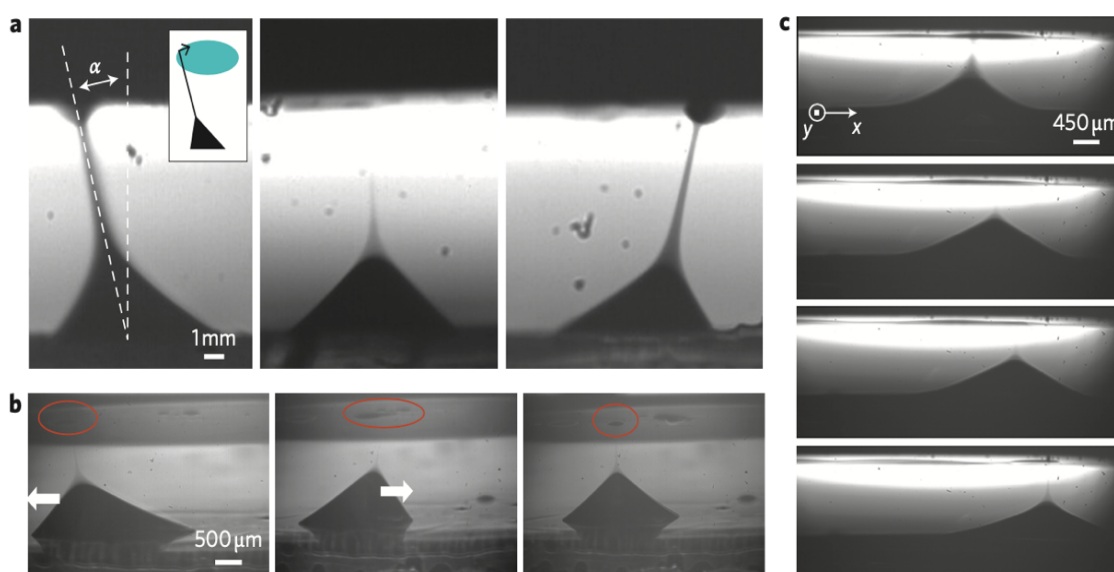


Fig.1.9: (a) Shooting of nanolitre almond oil droplets within a solid angle (off-axis directions up to ~ 208) from a standing sessile drop by moving the hot tip. The liquid was deposited over an area of $\sim 23 \text{ mm}^2$. (b, c) Shooting of almond oil droplets to different locations from a sessile drop (b), which is induced to translate onto the PDMS-coated glass by moving the hot tip beyond the threshold angle, and from a film (c), where the dispensing gun moves more easily and in two dimensions. (c) A lateral displacement of 1.6 mm along the x-axis is visible between the first (top) and last frames (bottom), and the translation of 1 mm along the y-axis is noticeable through the variation in image focus (Ferraro, P., Coppola, S., Grilli, S. *et al.* Dispensing nano-pico droplets and liquid patterning by pyroelectrodynamic shooting. *Nature Nanotech* 5, 429-435 [2010]).

The shooting function can also be synchronized harmonically with the displacement of the droplets while they are dispensed continuously (Fig.1.10a). The sequence of images in Fig.1.10a shows the formation of three droplets sliding to the right side. Such droplets could be collected and managed into a microfluidic system. This function is implemented by positioning the hot tip closer to the edge of the LN plate where the thermal dissipation, favoured by the contact with the glass spacer (see Fig.1.10b), generates colder regions. The 'dispensing and sliding effect' is driven by electrohydrodynamics (dispensing of droplets) and thermocapillarity (sliding of droplets to colder regions) activated simultaneously by a single external stimulus. The infrared laser beam offers several advantages over the hot tip. The temperature gradient induced by the laser can be varied quantitatively by modulating the laser power, and it is spatially highly selective. Beam focusing allows one to control and reduce the area to be stimulated. Figure 1.10 b, c shows side and perspective views of three drop reservoirs stimulated selectively and sequentially by the laser beam (red arrows, Fig.1.10b). The laser beam can be split into different directions to achieve simultaneous and parallel blasting from multiple guns for high-through-put dispensing processes¹⁵.

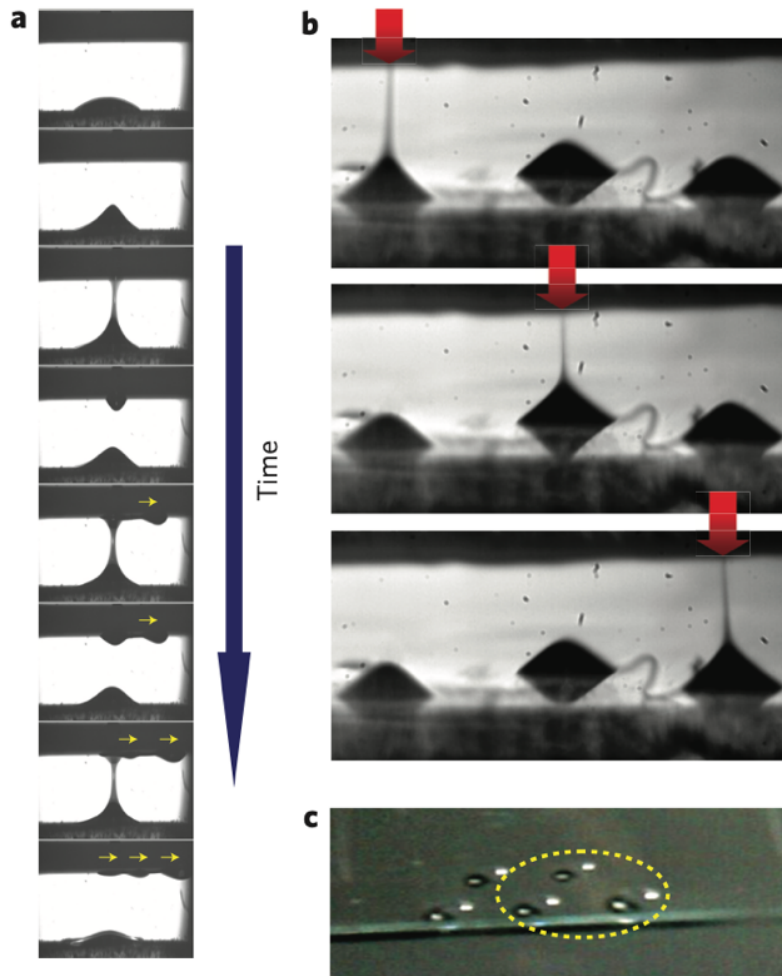


Fig.1.10: (a) Sequential images of the dispensing and successive lateral sliding of nanolitre droplets. (b) Sequential activation of three different drop reservoirs by the precise spatial scanning of the infrared laser beam. (c) Perspective image of five almond oil sessile drops on PDMS-coated glass (Ferraro, P., Coppola, S., Grilli, S. *et al.* Dispensing nano-pico droplets and liquid patterning by pyroelectrodynamic shooting. *Nature Nanotech* 5, 429–435 [2010]).

1.2.3 Liquid nanoprinting and patterning

The results show the possibility of drawing and dispensing liquid samples from a drop or film reservoir onto a functionalized substrate such as LN, with intriguing functionalities. However, the deposition of droplets directly onto the warm LN wafer causes spreading of the liquid due to the electrowetting effect caused by the uncompensated charges generated

pyroelectrically on the crystal surface. Moreover, the deposition of droplets onto chips other than the LN plate is desirable. The pyroelectrohydrodynamic dispenser was therefore improved according to the scheme presented in Fig.1.11a. Figure 1.11b shows a side view of the droplet dispensing onto the moving substrate. Figure 1.11c presents typical simple patterns printed by a carboxyl acid-based liquid (oleic acid), consisting of straight and curved continuous lines (width, ~40 μm) and separate droplets of different sizes (40 and 25 μm) and periods. Figure 1.11d shows periodic droplets printed by almond oil (up) and mineral oil (bottom), with diameters of ~200 and 15 μm , respectively. More complex patterns have been printed by mineral oil, including a continuous and dotted Greek fret (Fig.1.11e), a Greek fret with combined continuous and dotted lines (Fig.1.11f), a dotted staircase including a non-orthogonal angle (Fig.1.11g), a dotted staircase with smaller droplets (diameter, ~25 μm), in which the larger vertices were obtained by stopping the substrate during dispensing (Fig.1.11h), and a dotted staircase with further droplets and small vertices (droplet diameter, ~30 μm ; Fig.1.11i). Another intriguing functionality of the printing process consists in the simultaneous streaming of adjacent drop reservoirs with different volumes by the same thermal stimulus. A sort of multi-dispensing process is obtained that leads to the formation of parallel lines of droplets of two different diameters (Fig.1.11j).

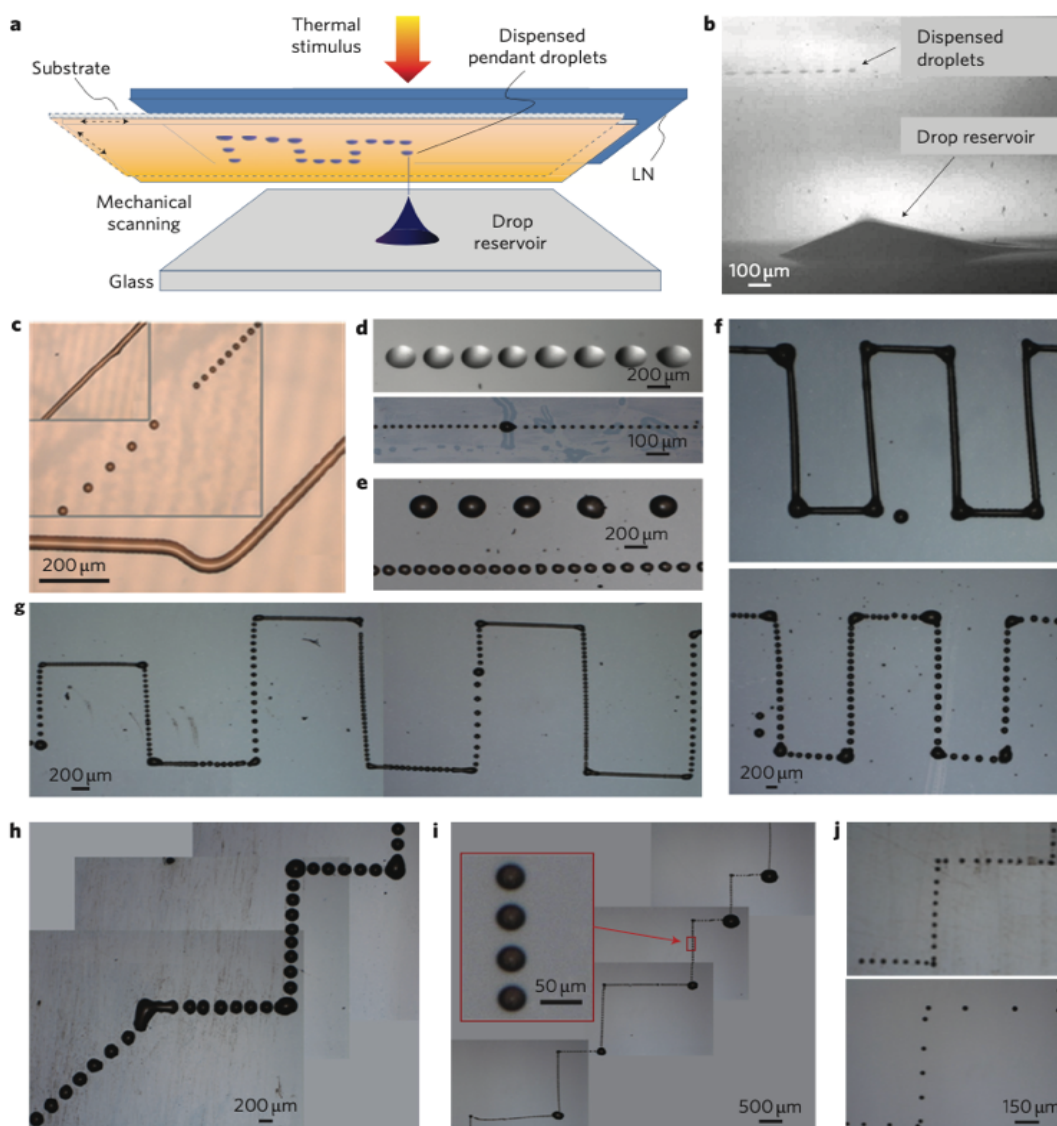


Fig.1.11: (a) Liquid is dispensed onto a translating substrate inserted between the LN and the glass plate. (b) Side view of the typical printing functionality. (c) Simple patterns printed by oleic acid: separate droplets, straight and curved lines. (d) Linear array of periodic separate droplets printed by almond oil (top) and mineral oil (bottom). (e) Two parallel printed lines obtained using two different adjacent drop reservoirs. (f) Continuous (top) and dotted (bottom) Greek fret printed by mineral oil. (g) Continuous and dotted patterned Greek fret. (h) Dotted staircase including a non-orthogonal angle. (i) Staircase with smaller droplets printed with large vertices. (j) Dotted staircase with small vertices. (Ferraro, P., Coppola, S., Grilli, S. *et al.* Dispensing nano-pico droplets and liquid patterning by pyroelectrodynamic shooting. *Nature Nanotech* 5, 429–435 [2010]).

It is important to point out that the technique is able to print droplets with much reduced dimensions by decreasing the volume of the drop reservoir (for example, after a certain number of shots). Figure 1.12a presents optical microscope images of tiny droplets of oleic acid dispensed from drop reservoirs of various volumes and dimensions (Fig.1.12b). The smallest dispensed droplets have volumes as low as ~ 3.6 μm^3 and radii of ~ 300 nm.

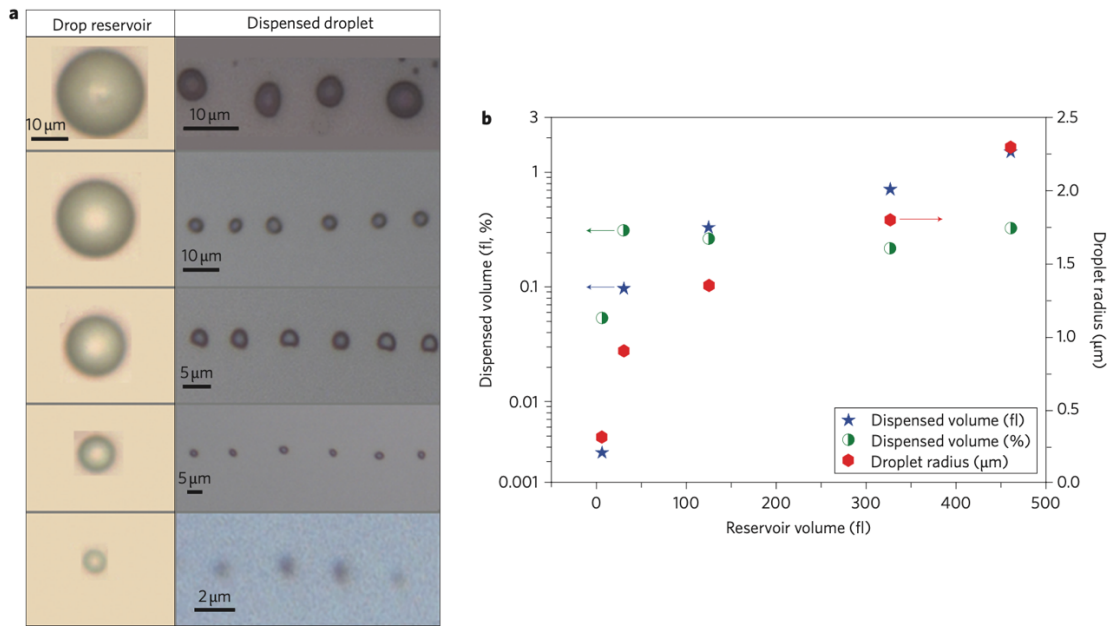


Fig.1.12: (a) Optical microscope images of different drop reservoirs and corresponding dispensed tiny droplets of oleic acid. (b) Corresponding volume and radius values of the dispensed droplets versus those of the reservoir in which the left y-scale is logarithmic (Ferraro, P., Coppola, S., Grilli, S. *et al.* Dispensing nano-pico droplets and liquid patterning by pyroelectrodynamics shooting. *Nature Nanotech* 5, 429-435 [2010]).

1.3 Dynamics in microfluidic system

Dynamics in microfluidic system can be analysed using various parameters such as: droplet inertia, gravity force, capillary forces, viscous forces, droplet velocity, solid surface properties, solid opening size and wettability. For the specific system geometry of this work other parameters are involved, such as the contact angle with the pin and the orifice.

In order to understand how a droplet interacts in a microfluidic system, a thorough study is needed.

1.3.1 Characteristic dimensionless numbers

The interactions between the various present forces can be analysed through some dimensionless numbers.

In order to relate inertia force to surface tension force, Weber Number is used when there is a separation surface between different fluids:

$$We = \frac{\rho \cdot U^2 l}{\sigma}$$

Where:

ρ is liquid density [Kg/m³];

U is the droplet approach velocity [m/s];

l is a characteristic length [m];

σ is surface tension [N/m].

In order to relate viscous drag force to surface tension force is used the Capillary Number. The Capillary number for a single flow formulation is:

$$Ca = \frac{\mu' \cdot U}{\sigma}$$

Where:

μ' is the dynamic viscosity of the liquid [N·s/m²];

U is the characteristic velocity [m/s];

σ is the surface tension [N/m].

Capillary number in multiphase flow has the same definition as the single flow formulation, the ratio of viscous to surface forces but has also the effect of the ratio of fluid viscosities:

$$Ca = \frac{\mu' \cdot U}{\sigma} \cdot \frac{\mu'}{\hat{\mu}}$$

Where:

μ' is the dynamic viscosity of the continuous phase;

$\hat{\mu}$ is the dynamic viscosity of the dispersed phase.

Instead, to relate inertia force to viscous drag force is used the Reynolds Number:

$$\text{Re} = \frac{\rho \cdot U \cdot l}{\mu'}$$

Where:

ρ is liquid density [Kg/m³];

U is the droplet approach velocity [m/s];

l is a characteristic length [m];

μ' is the dynamic viscosity of the liquid [N·s/m²].

On this way, Weber Number can also be expressed in function of the other two dimensionless groups as:

$$\text{We} = \text{Ca} \cdot \text{Re}$$

Therefore, it can be affirmed that in a microfluidic system when inertia force overcome surface tension force ($\rho U^2 l \gg \sigma$), the droplet goes through the system, while, in the opposite condition ($\rho U^2 l \ll \sigma$), there isn't flow.

However, in all microfluidic real systems, also the gravity interacts in the dynamics, so in order to express its contribution against the surface tension force, we use the Eötvös number (Eo), also called the Bond number (Bo):

$$\text{Eo} = \text{Bo} = \frac{\Delta\rho \cdot g \cdot l^2}{\sigma}$$

Where:

$\Delta\rho$ is difference in density of the two phases [kg/m³];

g is gravitational acceleration [m/s²];

l is characteristic length [m];

σ is surface tension [N/m].

A high value of the Eötvös or Bond number indicates that the system is relatively unaffected by surface tension effects; a low value (typically less than one) indicates that surface tension dominates.

1.3.2 Characteristic times

All the previously mentioned forces act in a specific characteristic time. Regarding the gravity force, its characteristic time can be expressed as:

$$t_g = \sqrt{\frac{\rho_l \cdot l}{\Delta\rho \cdot g}}$$

Where:

ρ_l is the liquid density [kg/m³];

l is a characteristic length [m];

$\Delta\rho$ is difference in density of the two phases [kg/m³];

g is gravitational acceleration [m/s²].

Instead, the characteristic time for capillary force is:

$$t_\sigma = \sqrt{\frac{\rho_l \cdot l^3}{\sigma}}$$

Where:

ρ_l is the liquid density [kg/m³];

l is characteristic length [m];

σ is surface tension [N/m].

In the end, the characteristic time for viscous force is:

$$t_{\mu} = \frac{\rho_l \cdot l^2}{\mu}$$

Where:

ρ_l is the liquid density [kg/m³];

l is characteristic length [m];

μ is the dynamic viscosity of the liquid [N·s/m²].

1.3.3 Droplet and surface properties in droplet Dynamics through an orifice¹⁶

Depending on the droplet initial velocity and surface properties, different regimes can occur (Fig.1.13). In case of hydrophobic hole there are three cases: NI, non-impregnation regime if the droplet velocity is low; LI, limited impregnation regime if the droplet has an intermediate velocity and SF, slug formation regime, i.e., the formation of a slug that disconnects from the upper part of the liquid, if the velocity is high. For a hydrophilic hole, if the droplet has low velocity it can wet the surface and pass through the hole, so a TI, total impregnation regime occurs; if the droplet has an intermediate velocity there is an air bubble formation between the droplet, B bubbling regime and, if the initial droplet velocity is high a SF regime occurs.

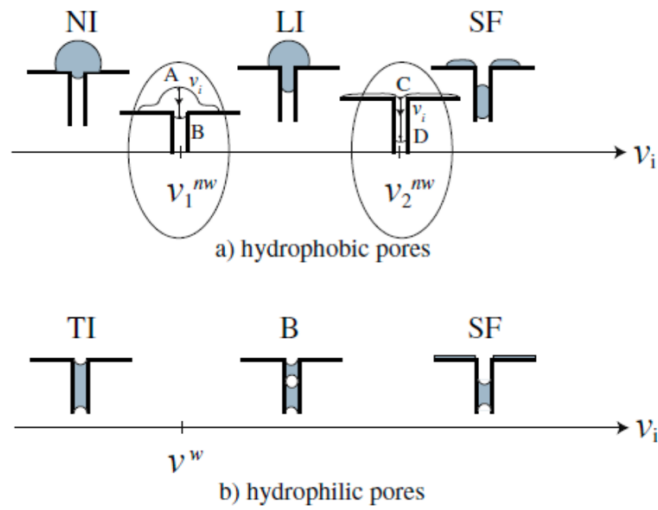


Fig.1.13: (a) Sketch of hydrophobic pores. (b) Sketch of hydrophilic pores. (Faraone A, Master Thesis: Dispensing pico droplets by pyroelectrohydrodynamic jetting: simulations and experimental results, 21-22 [2019]).

Surface wettability is another parameter that can affect the droplet dynamics. With the decrease of contact angle $\theta = 2\arctg(\frac{2H}{D})$, the droplet is easily captured, and there exists a critical equilibrium contact angle θ^{eq} when the Bond number and the orifice-to-droplet diameter ratio as well as the thickness of the plate are specified. For the case with $\theta > \theta^{eq}$, the droplet can finally pass through the orifice, otherwise, the droplet can't pass through the orifice.

After impact the droplet can either be captured above the surface or it can pass the orifice. This behaviour can be normalized with the tg . Results from the literature observable in Fig.1.14 show that for a droplet of water/glycerine in a tank filled with silicon oil, for the smaller orifice with $d/D = 0.54$, the maximum asymmetrical deformation occurs at $t=1.26tg$, after which the droplet retracts backward. When d/D increases, the droplet deformation is smaller and, after $t=1.26tg$, the lateral interface retraction leads to further penetration of the drop fluid into and through the orifice.

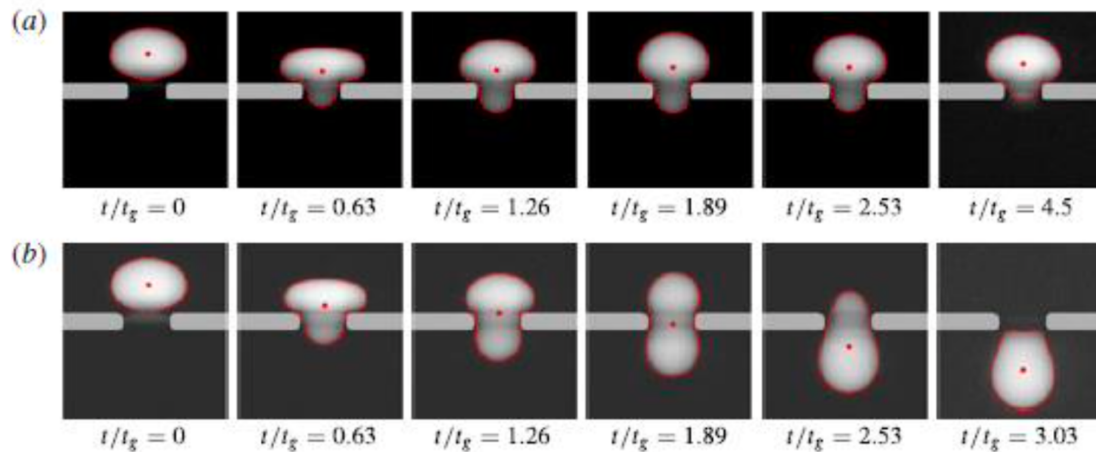


Fig.1.14: Time sequence of a drop through an orifice. (Faraone A, Master Thesis: Dispensing pico droplets by pyroelectrohydrodynamic jetting: simulations and experimental results, 21-22 [2019]).

Then, regarding the plate thickness, if the thickness is high, the hole behaves as capillary. Results obtained from a droplet of water/ glycerine in a tank filled with silicon oil at fixed contact angles, Bond number and orifice-to-droplet diameter ratio, shows that for a thickness of 8mm the droplet can pass the hole and go out, instead, for a plate thickness of 12mm the drop is not able to pass the hole.

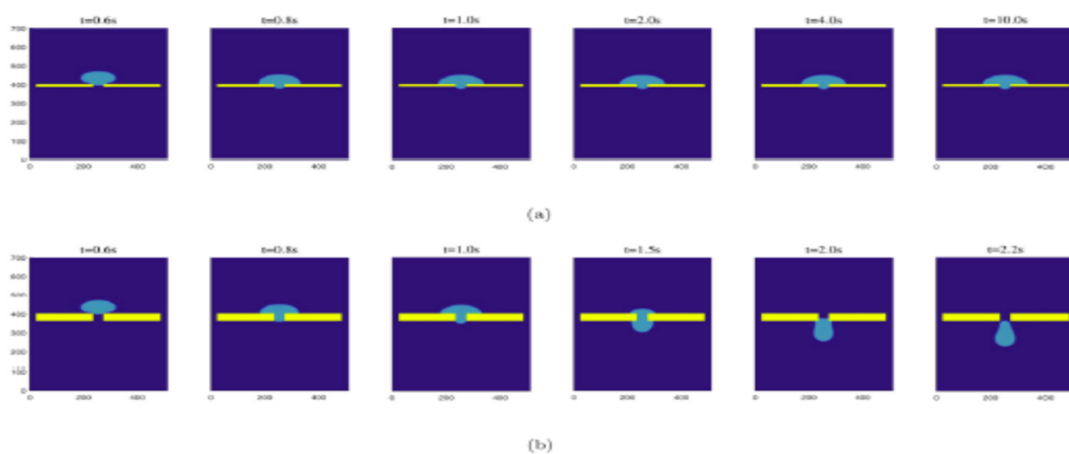


Fig.1.15: (a) Time sequence of a drop through an orifice with thickness of 8mm. (b) Time sequence of a drop through an orifice with thickness of 12mm. (Faraone A, Master Thesis: Dispensing pico droplets by pyroelectrohydrodynamic jetting: simulations and experimental results, 21-22 [2019]).

1.4 Previous study¹⁶

In last years, a lot of numerical simulations have been done in order to understand the droplets behaviour in microfluidic systems. Many of the best, according to the purpose of SensApp project, have involved the numerical simulations of droplet dynamics through an orifice system for pyroelectrodynamic shooting.

In this simulation, the geometry and a fine numerical mesh have been defined in COMSOL Multiphysics by adopting an axisymmetric geometry as reported in Fig.1.16, while to study meniscus formation and air-water interface, simulations were done in OpenFOAM.

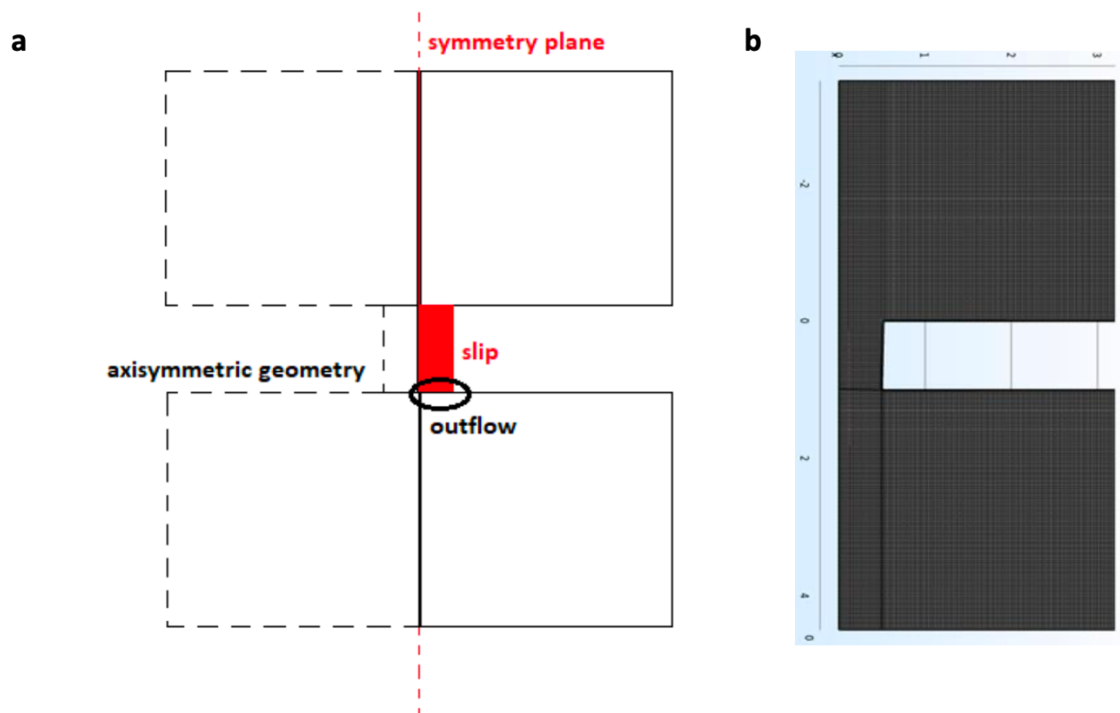


Fig.1.16: (a) Representation of axisymmetric geometry with boundary conditions and (b) mesh generated by COMSOL Multiphysics. (Faraone A, Master Thesis: Dispensing pico droplets by pyroelectrohydrodynamic jetting: simulations and experimental results, 21-22 [2019]).

Steady-state simulations have been performed by replacing the droplet dynamics in order to observe the thickness of drop meniscus and set the geometric parameters. The general scheme for geometry is reported in Fig.1.17, then, with a fixed contact angle (θ) of 60° , changes/variations have been applied to:

- channel radius;
- channel height;
- channel inclination angle;
- orifice and upper substrate wettability.

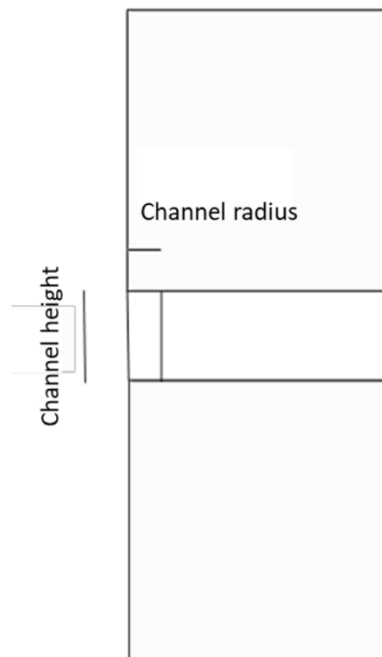


Fig.1.17: Input geometry of the work (Faraone A, Master Thesis: Dispensing pico droplets by pyroelectrohydrodynamic jetting: simulations and experimental results, 21-22 [2019]).

OpenFOAM simulations have been made on a water droplet initially spherical (or equivalently ellipsoidal) with different initial radius (or major and minor axes) in an air domain. Numerical simulations have

highlighted three different dynamics reported in Fig.1.18: one in which the meniscus formation is favoured, one in which the meniscus is initially formed but at the stationary it goes through the orifice and one in which the droplet goes through the orifice directly.

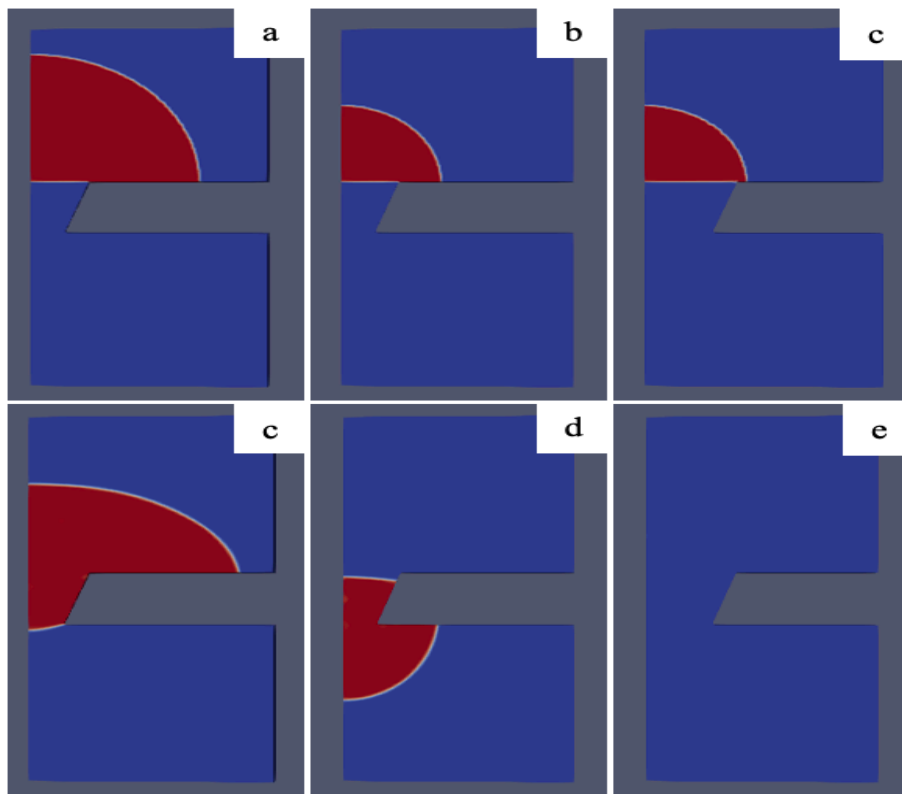


Fig.1.18: (a), (b), (c) Three droplets with different radius at $t=0$. (c) Meniscus formation at stationary referred to initial condition (a). (d) Slipping of the meniscus before the stationary referred to initial condition (b). (e) No formation of meniscus at stationary referred to initial condition (c). (Faraone A, Master Thesis: Dispensing pico droplets by pyroelectrohydrodynamic jetting: simulations and experimental results, 21-22 [2019]).

The results of this study are that meniscus formation is favoured for:

- high viscosity/low surface tension;
- small hole radius;
- high contact angle.

So, Since SensApp objective is the detection of small volume droplet, a meniscus thickness around $100 \mu\text{m}$ is the desired condition.

Based on this assumption and desiring to start with as small as possible droplet volume (that means small droplet radius), it can be concluded that the best meniscus thickness measure has been obtained in case of a droplet with 1mm radius goes through a channel with radius 0.5mm, height 1mm and inclination angle 40° .

Therefore, considering simulations results, the fabrication of a PMMA slide with an orifice having 0.3mm radius and inclination angle about 40° has been requested to VUB partner, but its fabrication it's not possible due to sensibility limit of the industrial machines used in this kind of manufacture.

1.5 Aim of the work

The aim of this thesis is to develop several simulations to analyse the behaviour of a droplet in an orifice-pin system in order to promote the meniscus formation in a possible industrial manufacture. The simulations have been performed varying various parameters such as characteristic length, contact angle with the pin, contact angle with the orifice, surface tension, kinematic viscosity and density.

The thesis is organized as follows: in Chapter 2 it's explained the mathematical method used to model the system and it's displayed the discretization used; in Chapter 3, in the first section simulations show the droplet dynamic varying non-physical properties of liquid (characteristic length, contact angle with the pin, contact angle with the orifice) at fixed kind of the droplet (distilled water); then, in the second section, simulations show droplet dynamic varying both non-physical properties (contact angle with the pin and contact angle with the orifice) and physical properties (kinematic viscosity, surface tension and density) at fixed characteristic length; finally in Chapter 4 some conclusions are made, concerning the influence of the different parameters on droplet behaviour too, and future perspective and possible significant consequences are considered.

CHAPTER 2

THE METHOD

This chapter shows the geometry of the system and explains the governing equations, the numerical method and the SensApp setup in order to understand how the dynamic of the droplet in an orifice-pin system have been studied.

2.1 Geometry

SensApp's real geometry used by CNR-ISASI is made up by an orifice and pin, as shown in Fig.2.1:

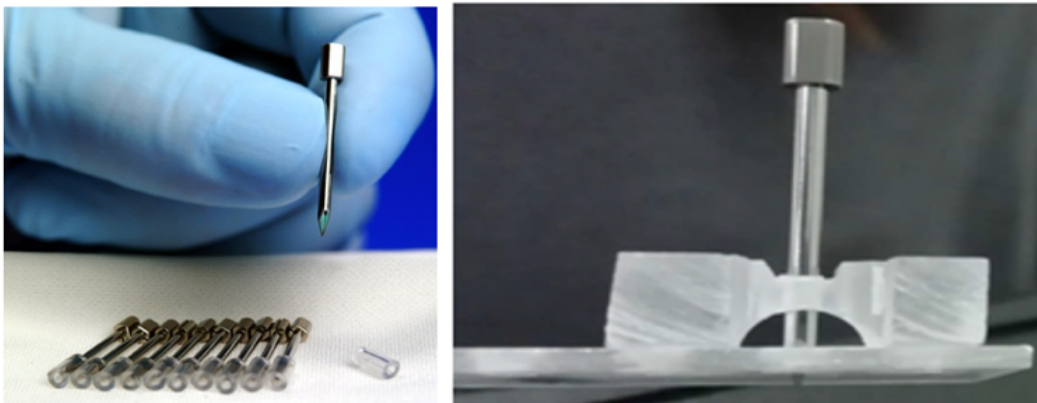


Fig.2.1: (a) Printing Pin; (b) combined system orifice-pin used for SensApp Project.

How can we see, the pin has got a particular geometry which in the simulations have been approximated to a hollow coaxial cylinder at the filled cylindrical pin structure (Fig.2.2). This has been made in order to use an axisymmetric geometry in the simulations in order to promote faster results.

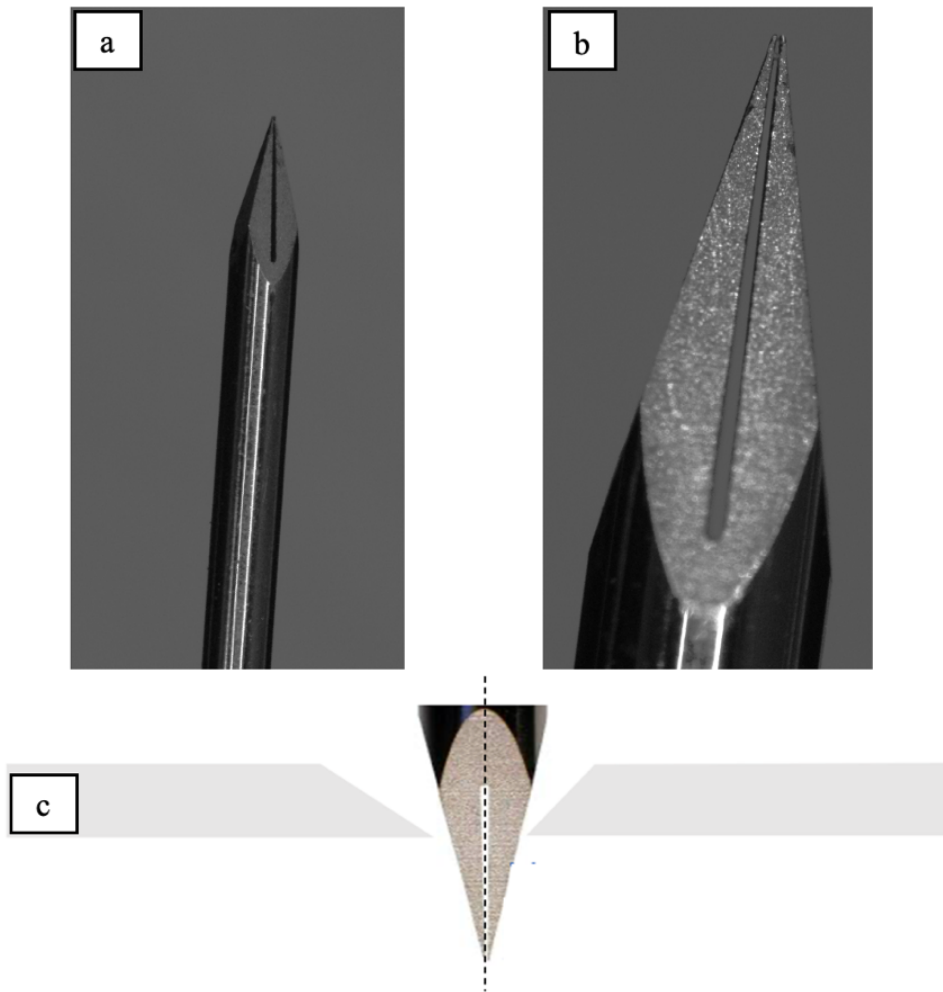


Fig.2.2: (a) Geometry of printing pin. (b) Zoom on the tip of the printing pin. (c) Axisymmetric cut used in the simulations.

On these assumptions, the geometry used in simulations is characterized by $D_t = 5$ mm (the top orifice diameter), $D_b = 1$ mm (bottom orifice diameter), $T = 3.5$ mm (the thickness), $\alpha = 60.25^\circ$ (the cone inclination), $R_1 = 40$ μm (characteristic dimension of the capillary), $L_c = 2$ mm (capillary length), $L_t = 2.3$ mm (the tip length), $D_1 = 200$ μm (the space between the orifice bottom diameter and the printing pin) and $D_2 = 1.1$ mm (the pin length exiting from the orifice).

Geometry used in simulations is shown in Fig.2.3.

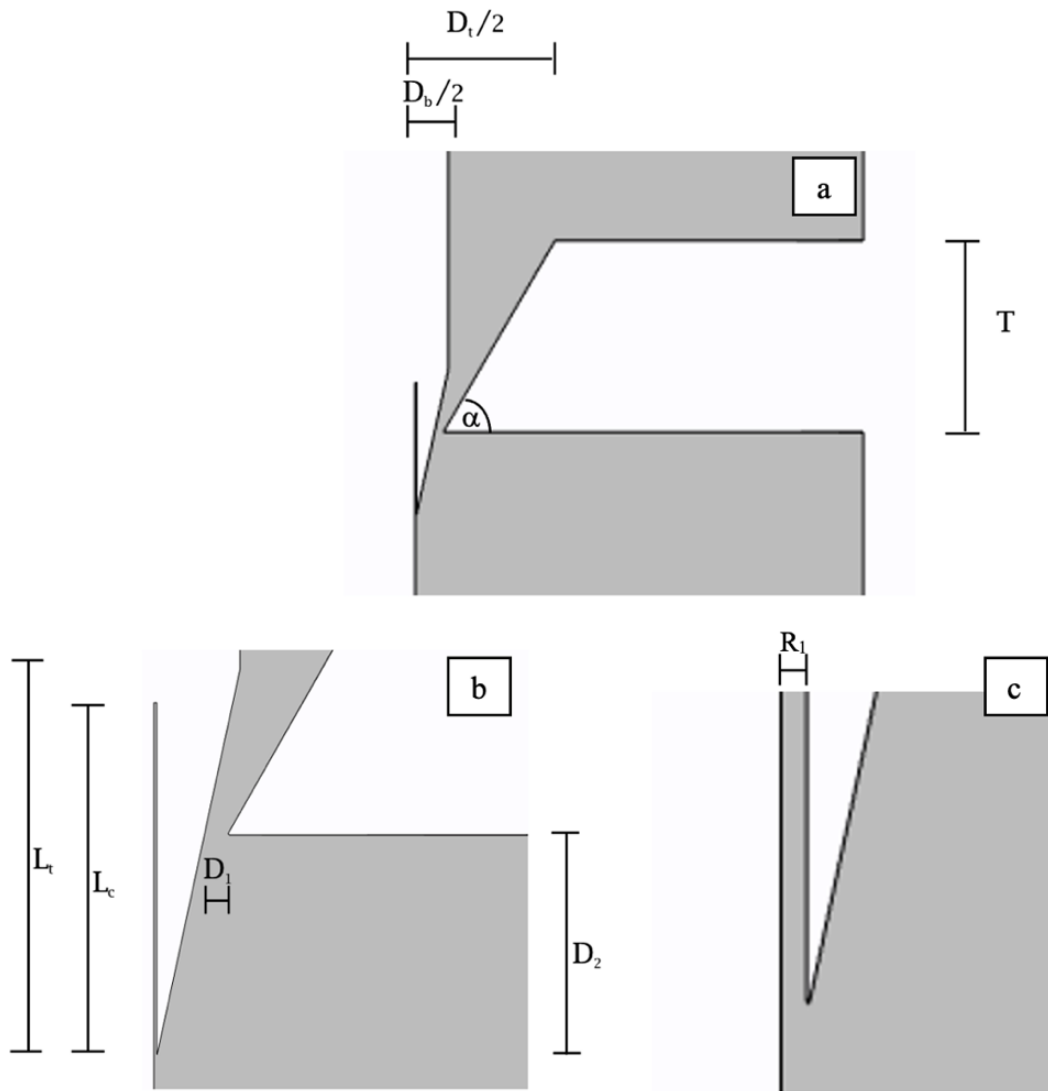


Fig.2.3: (a) Dimensions of the orifice; (b),(c) Dimensions of the pin and the system orifice-pin.

2.2 Mathematical model

Here, it will be considered a liquid-air system in which fluids are Newtonian incompressible fluids in isothermal condition.

In general, the momentum conservation equation and the incompressibility constraint are expressed as:

$$\nabla \cdot \mathbf{u} = 0 \quad (1)$$

$$\rho \left(\frac{\partial \mathbf{u}}{\partial t} + \mathbf{u} \cdot \nabla \mathbf{u} \right) = \nabla \cdot \mathbf{T} + \mathbf{F} \quad (2)$$

Where u is the velocity vector, \mathbf{T} is the stress tensor and \mathbf{F} the contribution of mass forces. In this case, the stress tensor is $\mathbf{T} = -\nabla p + \eta \nabla^2 \mathbf{u}$ with p pressure and η viscosity, while the mass force is the gravity force, so $\mathbf{F} = \rho \mathbf{g}$ with ρ density and \mathbf{g} gravity acceleration.

In particular, momentum conservation equation and the incompressibility constraint of Newtonian incompressible fluids in isothermal condition are the Navier-Stokes's equations:

$$\nabla \cdot \mathbf{u} = 0 \quad (1)$$

$$\rho \left(\frac{\partial \mathbf{u}}{\partial t} + \mathbf{u} \cdot \nabla \mathbf{u} \right) = -\nabla p + \eta \nabla^2 \mathbf{u} + \rho \mathbf{g} \quad (2)$$

To study droplet meniscus formation and air-water interface, the transport equation is:

$$\frac{\partial \alpha}{\partial t} + \nabla \cdot (\mathbf{u} \alpha) = 0 \quad (3)$$

In which the phase fraction α takes values ranging externally from 0 to 1 ($0 \leq \alpha \leq 1$), where 0 and 1 correspond to regions accommodating only one phase, e.g., $\alpha=0$ for gas and $\alpha=1$ for liquid. Accordingly, gradients of the phase fraction are encountered only in the region of the interface.

To solve the balance and constitutive equations, we need to add the boundary conditions. In this case, as shown in Fig.2.4, we refer to:

- inflow on the upper boundaries;
- outflow on the bottom boundaries and upper internal boundary of the pin;
- axial symmetry on the axis of symmetry;
- slip with a prescribed contact angle on the walls (of the pin and of the orifice).

Inflow condition used is:

$$\mathbf{u}|_{t=0} = 0 \quad (4)$$

Outflow condition used is the Neumann condition:

$$\mathbf{T} \cdot \mathbf{n} = -p_{\text{out}} \mathbf{n} \quad (5)$$

where \mathbf{n} is the normal out of the boundary and p_{out} is a known pressure value at the outlet (atmospheric pressure).

Instead, the axial simmetry condition is:

$$\begin{cases} \mathbf{u} \cdot \mathbf{n} = 0 \\ (\mathbf{I} - \mathbf{nn}) \cdot (\mathbf{T} \cdot \mathbf{n}) = 0 \end{cases} \quad (6)$$

where $\mathbf{I} \equiv \delta_{ij}$.

The general slip condition on the walls is:

$$\begin{cases} \mathbf{u} \cdot \mathbf{n} = 0 \\ (\mathbf{I} - \mathbf{nn}) \cdot (\mathbf{T} \cdot \mathbf{n}) = \beta (\mathbf{I} - \mathbf{nn}) \cdot (\mathbf{u} - \mathbf{u}_{\text{wall}}) \end{cases} \quad (7)$$

however, it gets particularized varying the β factor in function of the contact angle with the walls. His variation is between 0 (perfect slip condition, that is when no shear stresses are present) and ∞ (no-slip condition, that is when $\mathbf{u} = \mathbf{u}_{\text{wall}}$).

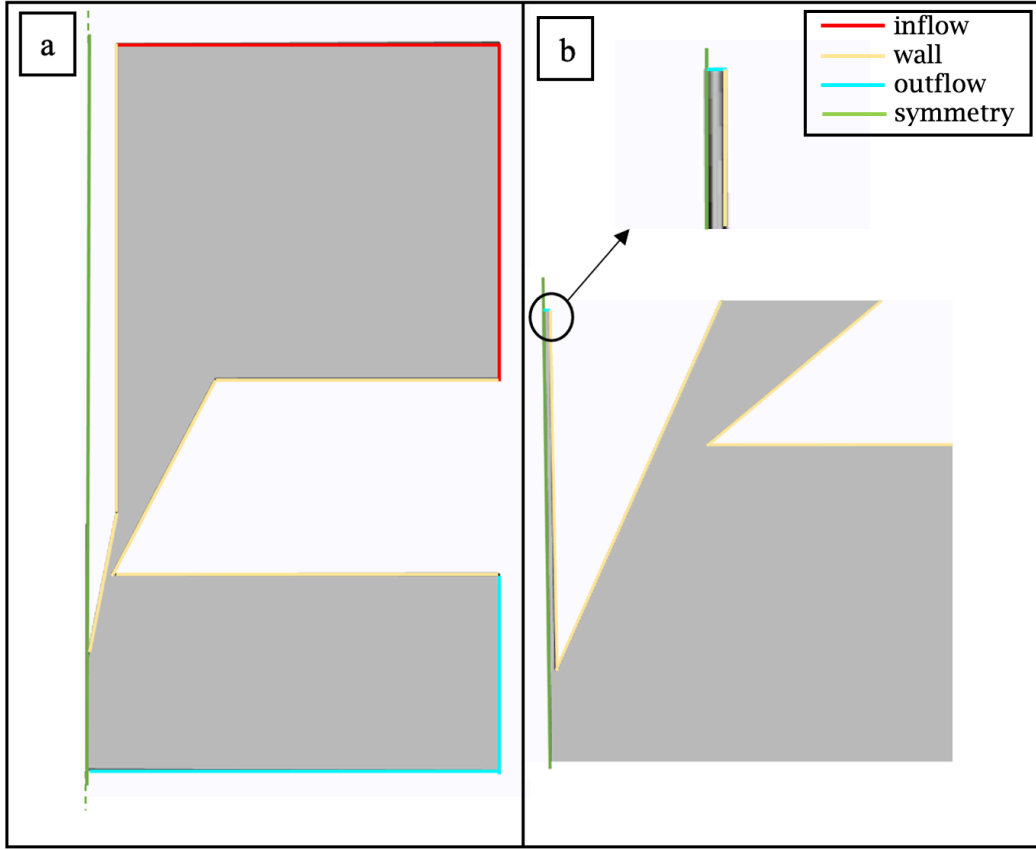


Fig.2.4: (a) Boundary conditions for combined system orifice-pin. (b) Zoom on boundary conditions of the internal boundaries of the pin.

Regarding the liquid-air interface, expressing with “l” and “a” the subscripts respectively, the conditions are:

$$\mathbf{u}_l = \mathbf{u}_a \quad (8)$$

$$(\mathbf{T}_1 - \mathbf{T}_2) \cdot \mathbf{n} = \Gamma \mathbf{n} \nabla \cdot \mathbf{n} \quad (9)$$

However, because of we want to highlite the effect of dimensionless parameters, we express the Navier-Stokes equations in dimensionless way:

$$\frac{\partial \mathbf{u}^*}{\partial t} + \mathbf{u}^* \nabla^* \mathbf{u}^* = - \frac{1}{Fr^2} \nabla^* z^* - \nabla^* p^* + \frac{1}{Re} \nabla^{*2} \mathbf{u}^* \quad (10)$$

In which the * suffix indicates the corresponding dimensionless of the analyzed parameters and the Fr is the Froude dimensionless number:

$$Fr = \frac{\mathbf{u}}{\sqrt{gl}}$$

Nevertheless, the Fr can be expressed also in function of other dimensionless numbers as:

$$\text{Fr}^2 = \frac{\text{We}}{\text{Bo}} = \frac{\text{Re} \cdot \text{Ca}}{\text{Bo}}$$

On this way, the Navier-Stokes equations with the analysed dimensionless numbers in this thesis are:

$$\frac{\partial \mathbf{u}^*}{\partial t} + \mathbf{u}^* \nabla^* \mathbf{u}^* = - \frac{\text{Bo}}{\text{Re} \cdot \text{Ca}} \nabla^* z^* - \nabla^* p^* + \frac{1}{\text{Re}} \nabla^{*2} \mathbf{u}^* \quad (11)$$

For the same reason, we express also the liquid-air equation (9) as well:

$$\left(\nabla^* p_l^* + \frac{1}{\text{Re}} \nabla^{*2} \mathbf{u}_l^* \right) \cdot \mathbf{n} = \left(\nabla^* p_a^* + \frac{1}{\text{Re}} \nabla^{*2} \mathbf{u}_a^* \right) \cdot \mathbf{n} \quad (12)$$

2.3 Numerical discretization

For the solution of the equations listed and the study of meniscus formation in an orifice-pin system, simulations were performed in OpenFOAM, while the geometry and the mesh have been defined in COMSOL Multiphysics. OpenFOAM is the leading free, open source software for computational fluid dynamics (CFD), owned by the OpenFOAM Foundation and distributed exclusively under the General Public Licence (GPL). The GPL gives users the freedom to modify and redistribute the software and a guarantee of continued free use, within the terms of the licence¹⁷.

OpenFOAM is based on the Finite Volume Method, so Volume-Of-Fluids (VOF) simulations were done in it.

2.3.1 Volume discretization

The Newtonian fluids domains are discretized using the finite element method employing a quadratic tetrahedra. The size of the mesh is calibrated for fluid dynamics extra fine for all domain, while is finest for the space between pin and orifice in order to have a better discretization of the liquid-air interface.

The mesh used is shown in Fig.2.5:

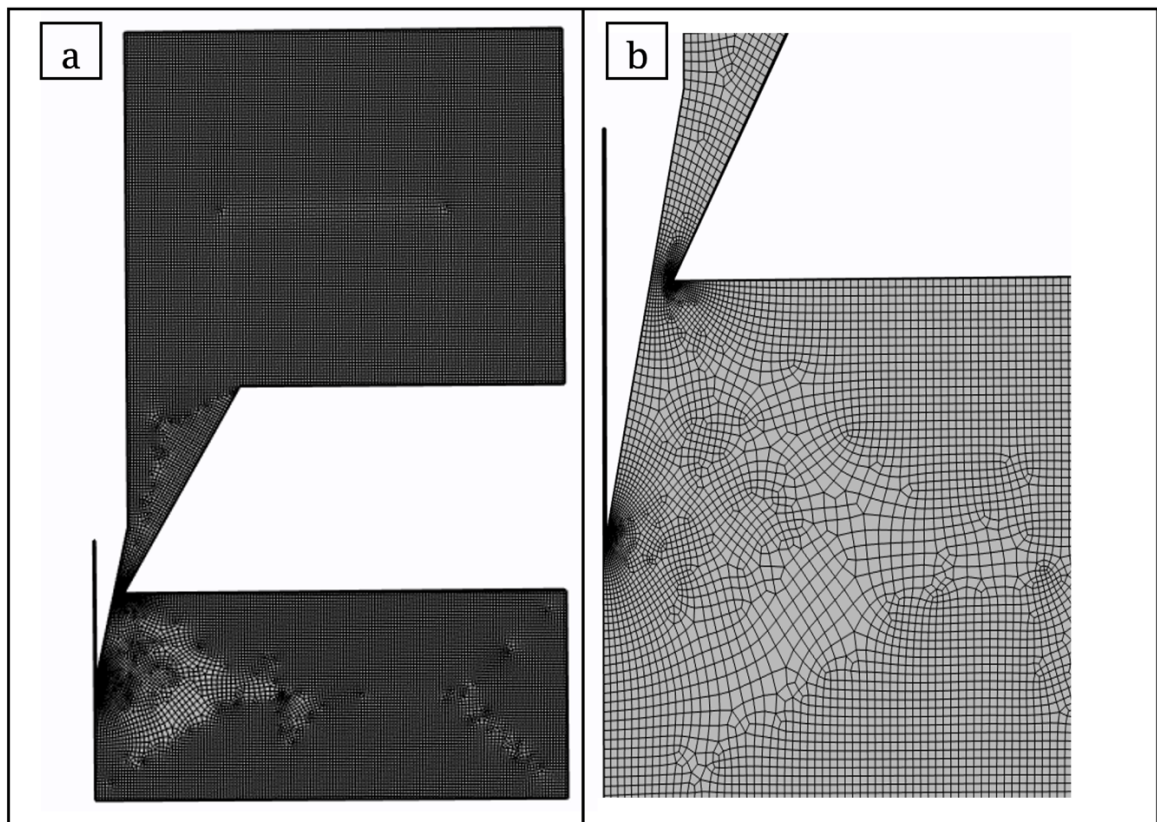


Fig.2.5: (a) Mesh of all domains. (b) Mesh zoom on the space between pin and the orifice.

In order to avoid numerical problems, some angles have been approximated to broken lines (Fig.2.6).

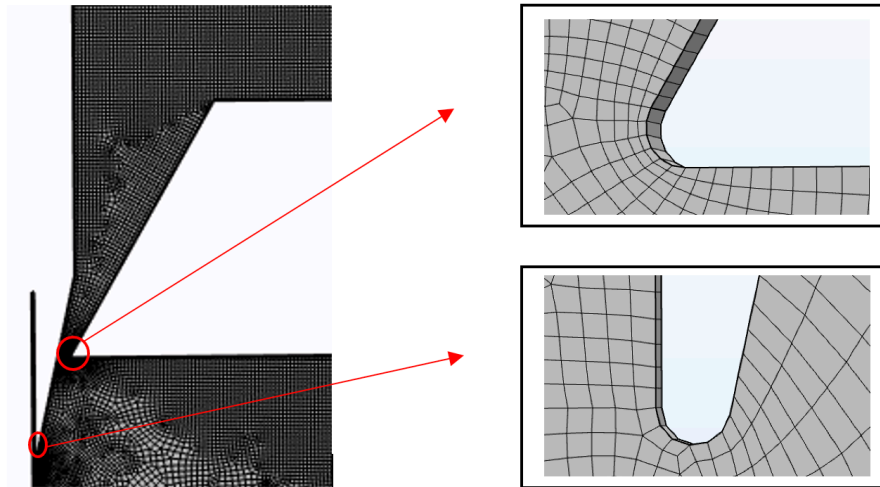


Fig.2.6: Approximation of angles in broken lines.

To make the mesh compatible with OpenFOAM, a revolve angles of 5° is needed to the 2D geometry (Fig.2.7). While, in order to import the mesh in OpenFOAM, some file conversions have been made from the .mph format to .foam format.

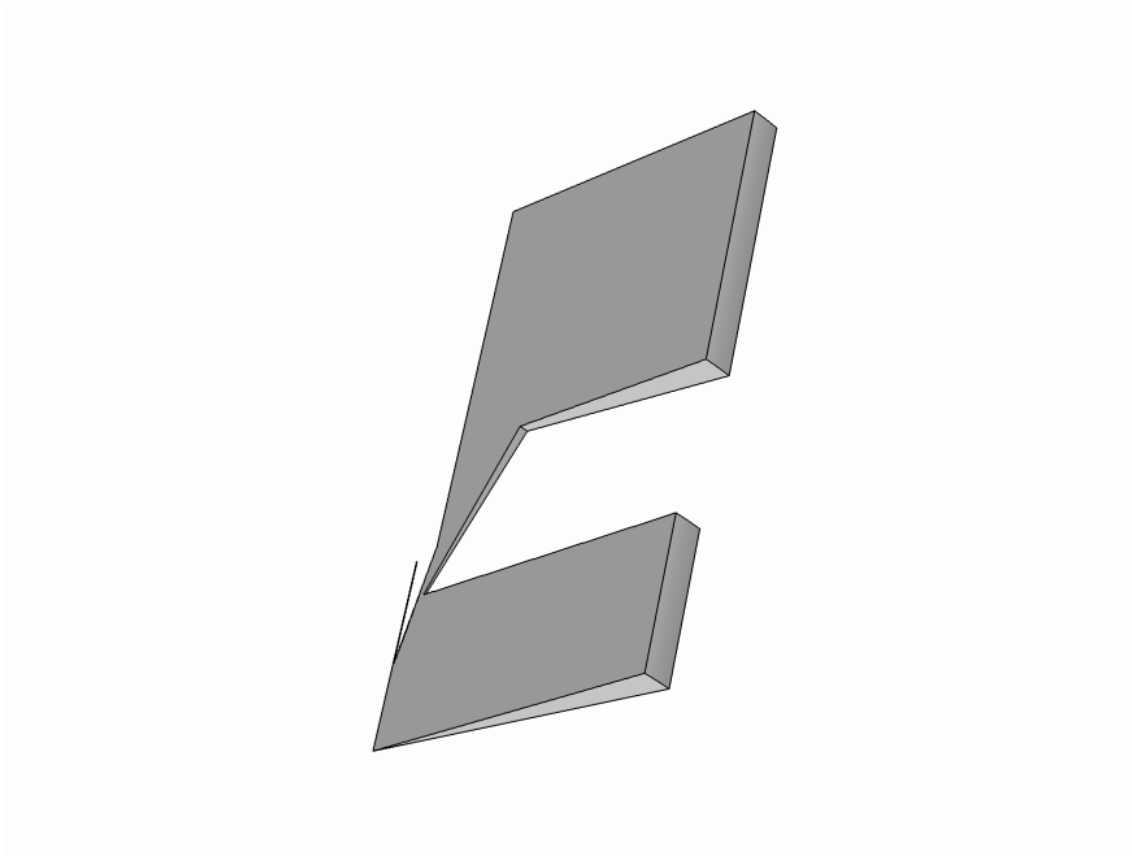


Fig.2.7: Revolve angles of 5° for current geometry.

2.3.2 Time stepping and computational time

Before running simulations we have to point out what time stepping scheme we want to involve. The considered time is divided into discrete intervals using a timestep Δt . In the simulations the time stepping scheme used has been performed using $\Delta t = 0.000001$.

The simulations of the droplet dynamic in an orifice-pin system are performed on 1 core of a blades DELL Power Edge M710HD with two hexacore processors Intel Xeon E5649 @ 2.53 GHz and 48 GB of RAM.

The computational time ranges from twelve hours to fifteen days.

2.4 SensApp set up¹⁶

The pyro-electrohydrodynamic-jet (p-jet) is a radically innovative method that uses the pyroelectric effect to produce tiny droplets (down to about 10^{-6} pL). A pyroelectric slab is able to generate a charge density on the surface when subjected to a transient and slight temperature (T) gradient. The resulting electric field causes the ejection of tiny droplets from the mother drop. The p-jet draws daughter droplets directly from the meniscus of the mother drop pipetted by the operator on the loading support (e.g. 2 μ L), producing the smallest volumes.

A schematic set-up configuration for an orifice system, called “top-down”, is reported in Fig.2.8:

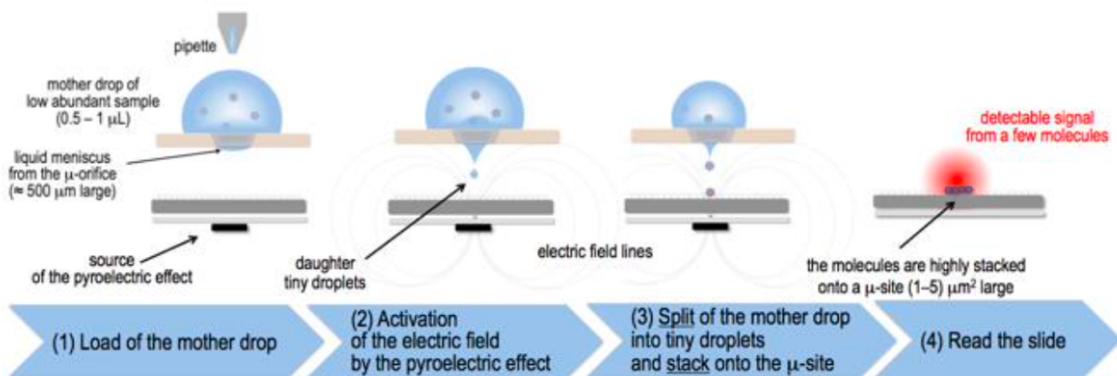


Fig.2.8: Top-down set-up.

It is possible to observe that a mother drop of sample is loaded on the engineered μ -orifice of the loading support to form a thin liquid meniscus on the opposite face. A slab (reaction support) is functionalized by immobilizing the appropriate antibody (high density and high affinity with the antigen in sample) and faces the μ -orifice. A pyroelectric slab, functionalized by a point-wise thermal source aligned with the μ -orifice, works as source of the pyro-electrohydrodynamic jet (p-jet) that triggers the rapid dispensing of tiny daughter droplets onto the same site (' μ -site') of the reaction support. For simplicity, the antigen molecules in Fig.2.8 are fluorescent but, in reality, they are labelled by secondary reactions after stacking.

Actual set-up of pyro-electrohydrodynamic system is similar to that reported with the μ -heater in the opposite position. It is constituted by a μ -heater realized in Tungsten, a LN slide, a receiver amino substrate, and a loading support made by a polymer, such as PMMA with the μ -orifice. The approach for the combined orifice-pin system is the same.

2.4.1 Heat transfer devices

In order to generate the pyroelectric effect, it is necessary to apply a temperature gradient on LN slide. According to First Joule Law $P=V \cdot I$, an electrical circuit has been used with the aim to obtain a thermal power. μ -

heater (see Fig.2.9) has been fabricated in lab workshop with a Tungsten wire having $300\mu\text{m}$ diameter. The final shape is dictated by the need to have a pointed stimulus.

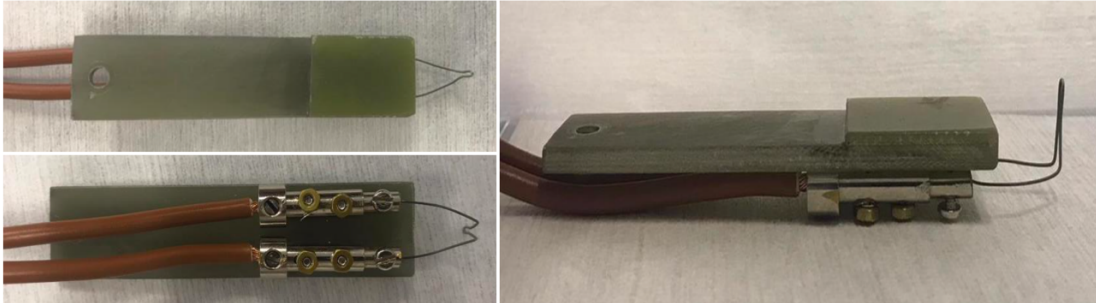


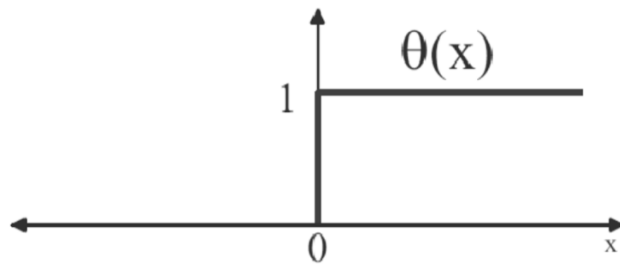
Fig.2.9: Top and side picture of μ -heater.

The electrical circuit is set by enabling the power supply (Lab. Grade Switching Mode Power Supply HCS-3300 in Fig.2.10) and a waveform generator (33220A Function / Arbitrary Waveform Generator, 20 MHz see Fig.2.10) is utilized to set a unit step function with assigned on and off times.



Fig.2.10: Power supply and waveform generator.

The choice of a unit step function is governed by the necessity to have a predefined period in which the current passage is assured/enabled, and another period without current in order to activate and deactivate the μ -heater with a fixed time lapse. The input function is a discontinuous function with zero values for negative arguments, corresponding to absence of current in the μ -heater and one for positive arguments, matching the current passage.



Then a fan cooler is positioned in the bottom of the set up.

CHAPTER 3

NUMERICAL SIMULATIONS OF DROPLET DYNAMICS THROUGH AN ORIFICE-PIN SYSTEM

In this chapter, the behaviour of a droplet, initially spherical, in an orifice-pin system is investigated. The aim of this chapter is to report the results of simulations in which have been varied the contact angles with the walls: at first, varying the characteristic length, and after the physical properties of the liquid. The desired condition is that in which the droplet goes through the orifice-pin system and creates a meniscus shape on the tip of the printing pin.

3.1 Simulations of distilled water droplet through an orifice-pin system

First simulations have been performed considering distilled water as liquid. On this assumption, the physical properties considered are:

PHYSICAL PARAMETERS (WATER/AIR SYSTEM)	
Droplet Viscosity	$1 \cdot 10^{-6} \text{ m}^2/\text{s}$
Droplet Density	$1000 \text{ kg}/\text{m}^3$
Surface Tension	$0.07 \text{ N}/\text{m}$
Air Density	$1 \text{ kg}/\text{m}^3$
Air Viscosity	$1.48 \cdot 10^{-5} \text{ m}^2/\text{s}$

and the involved dimensionless numbers are $Re = 1.928$, $Ca = 1.42 \cdot 10^{-5}$ and $Bo = 0.521$ (considering $u = 0.001 \text{ m}/\text{s}$ as average velocity and $l = 0.001928$ as characteristic length).

3.1.1 Simulations on CNR's standard geometry

In these simulations, the geometry used was the one described in the past chapter and the only changed quantities are the contact angle with the pin and the radius of the droplet, while the contact angle with the orifice has been set at 60°.

On this way, the analysed cases are those of Fig.3.1.

Contact angle with the orifice	Radius of the droplet [mm]	Contact angle with the pin
60°	[~1; 3; 4]	[5°; 10°; 15°; 20°; 25°; 30°; 35°; 40°; 45°; 50°; 55°, 60°]

Fig.3.1: Analysed values during the simulations.

The initial positions used are those in which the droplet is positioned between orifice and pin space as shown in Fig.3.2.

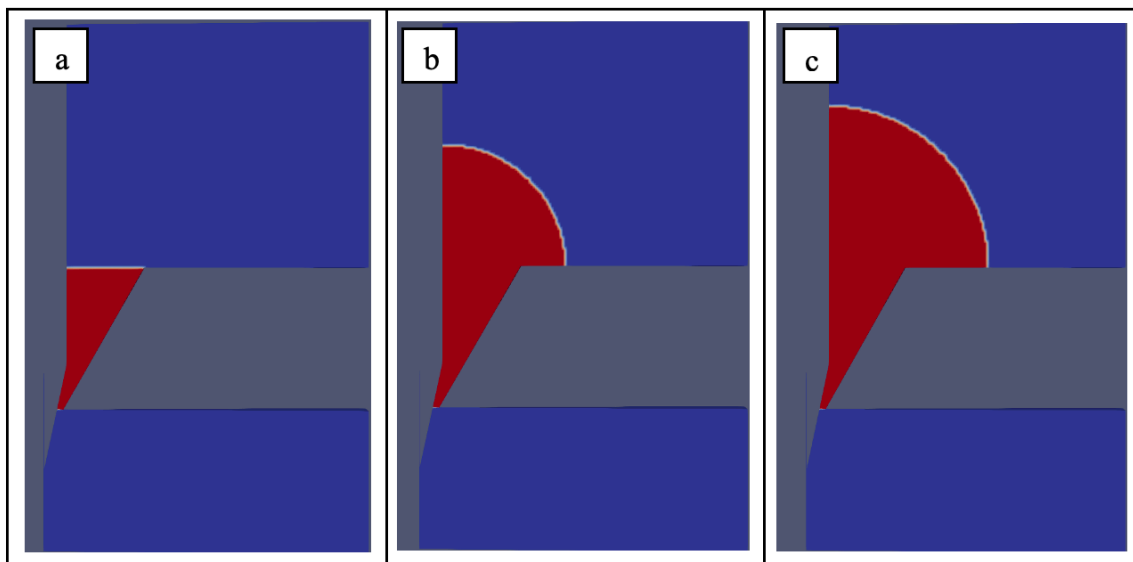


Fig.3.2: (a) Initial shape with $r \sim 1$ mm; (b) Initial shape with $r = 3$ mm; (c) Initial shape with $r = 4$ mm.

Varying the contact angle with the pin θ (Fig.3.3), the simulations have shown the following stationaries for the droplet with $r \sim 1$ mm.

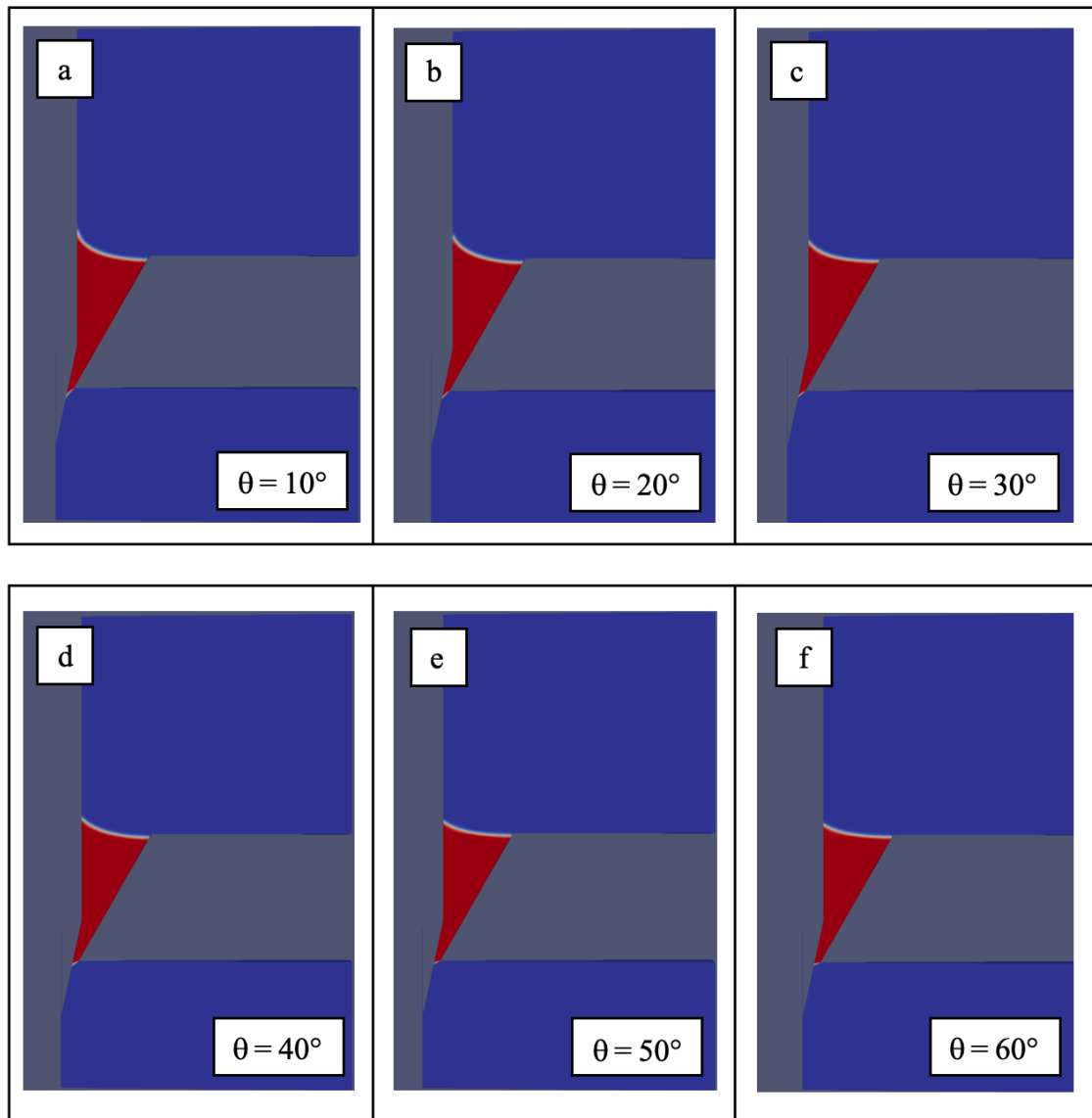


Fig.3.3: Simulations performed with a contact angle with the orifice of 60° , $r \sim 1$ mm and different contact angle with the pin. (a) Simulation with $\theta = 10^\circ$; (b) Simulation with $\theta = 20^\circ$; (c) Simulation with $\theta = 30^\circ$; (d) Simulation with $\theta = 40^\circ$; (e) Simulation with $\theta = 50^\circ$; (f) Simulation with $\theta = 60^\circ$.

Others contact angles with the pin show similar conditions to those of Fig.3.3.

How can we see, the droplet is not able to pass through the system.

Using a droplet with $r = 3$ mm, the same investigation has been performed. The simulations have shown the dynamics of Fig.3.4.

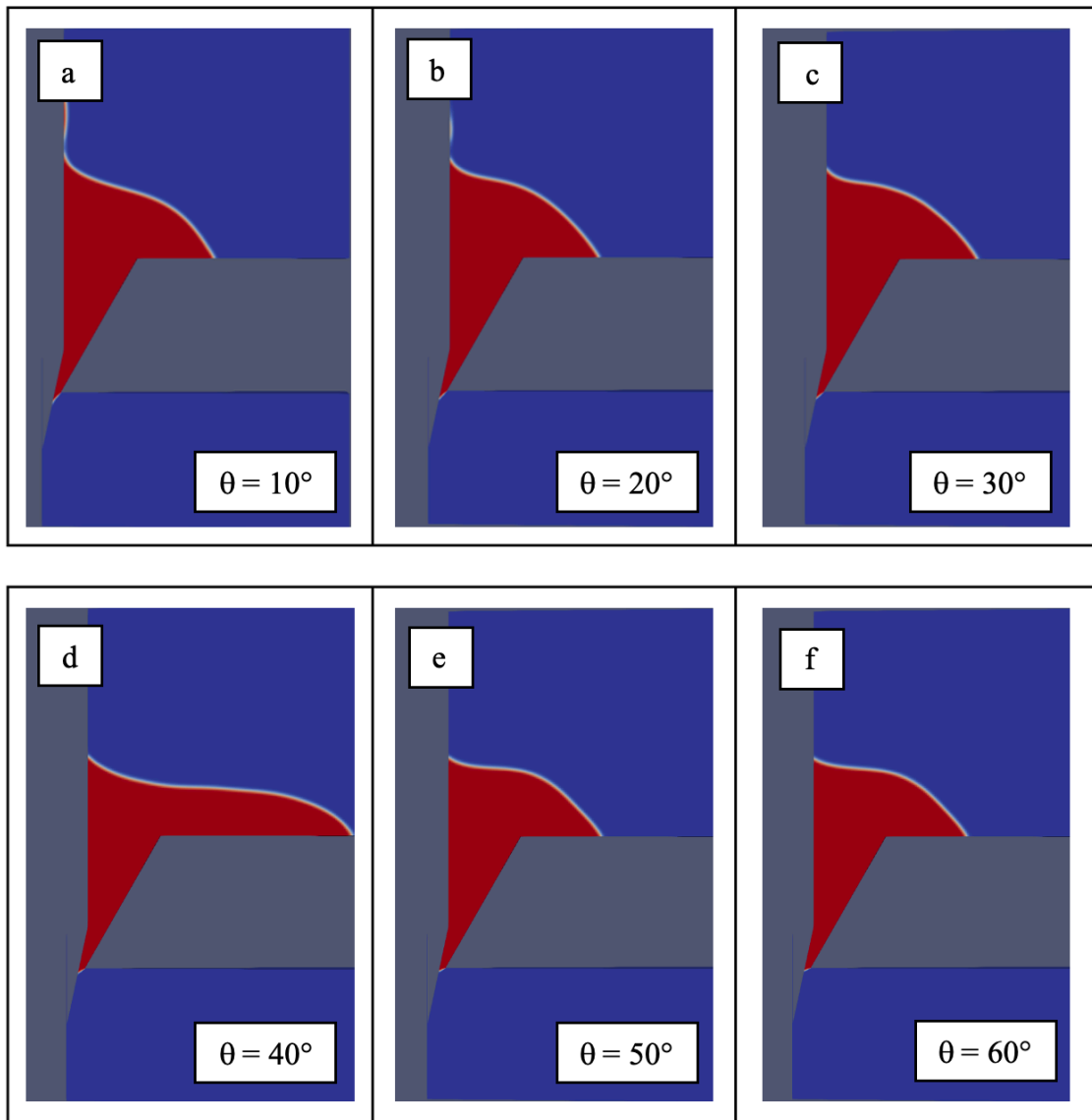


Fig.3.4: Simulations performed with a contact angle with the orifice of 60° , $r = 3$ mm and different contact angle with the pin. Every frame shows the situation at $t = 0.035$ s. (a) Simulation with $\theta = 10^\circ$; (b) Simulation with $\theta = 20^\circ$; (c) Simulation with $\theta = 30^\circ$; (d) Simulation with $\theta = 40^\circ$; (e) Simulation with $\theta = 50^\circ$; (f) Simulation with $\theta = 60^\circ$.

Others contact angles with the pin show similar conditions to those of Fig.3.4.

Although the dynamics are different before the stationary, the droplet is still not able to pass through the system.

To complete the cases, the investigation has been made also for a droplet with $r = 4$ mm and the frames are in Fig.3.5.

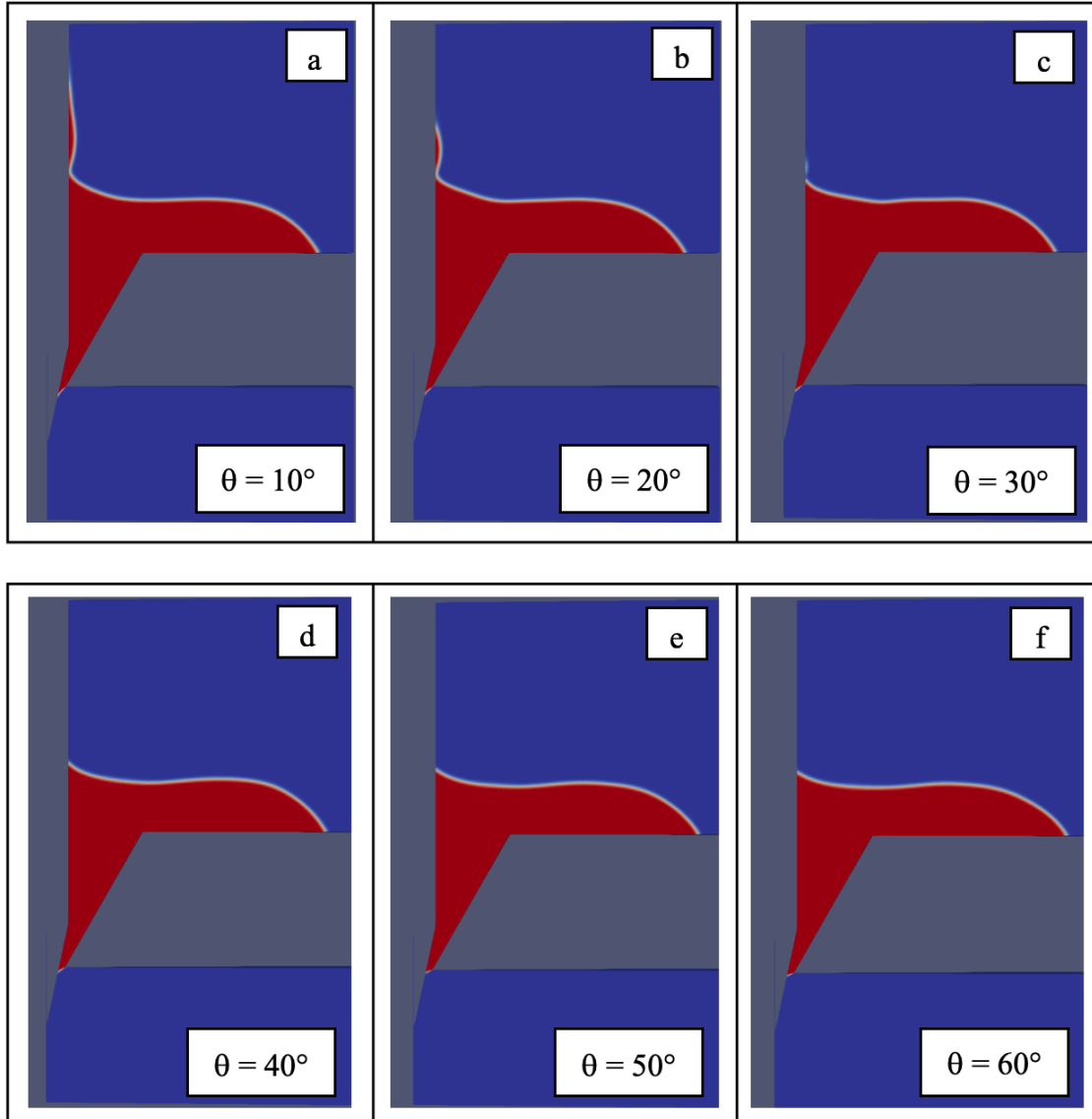


Fig.3.5: Simulations performed with a contact angle with the orifice of 60° , $r = 4$ mm and different contact angle with the pin. Every frame shows the situation at $t = 0.035$ s. (a) Simulation with $\theta = 10^\circ$; (b) Simulation with $\theta = 20^\circ$; (c) Simulation with $\theta = 30^\circ$; (d) Simulation with $\theta = 40^\circ$; (e) Simulation with $\theta = 50^\circ$; (f) Simulation with $\theta = 60^\circ$.

Others contact angles with the pin shows similar conditions to those of Fig.3.5.

Although the dynamics are different before the stationary, also in this case, the droplet is still not able to pass through the system.

In every simulation done considering the parameters listed before, the droplet is not able to pass through the space between the orifice and the pin. Furthermore, the common stationary position of the bottom of the droplet for all analysed cases is specified in Fig.3.6.

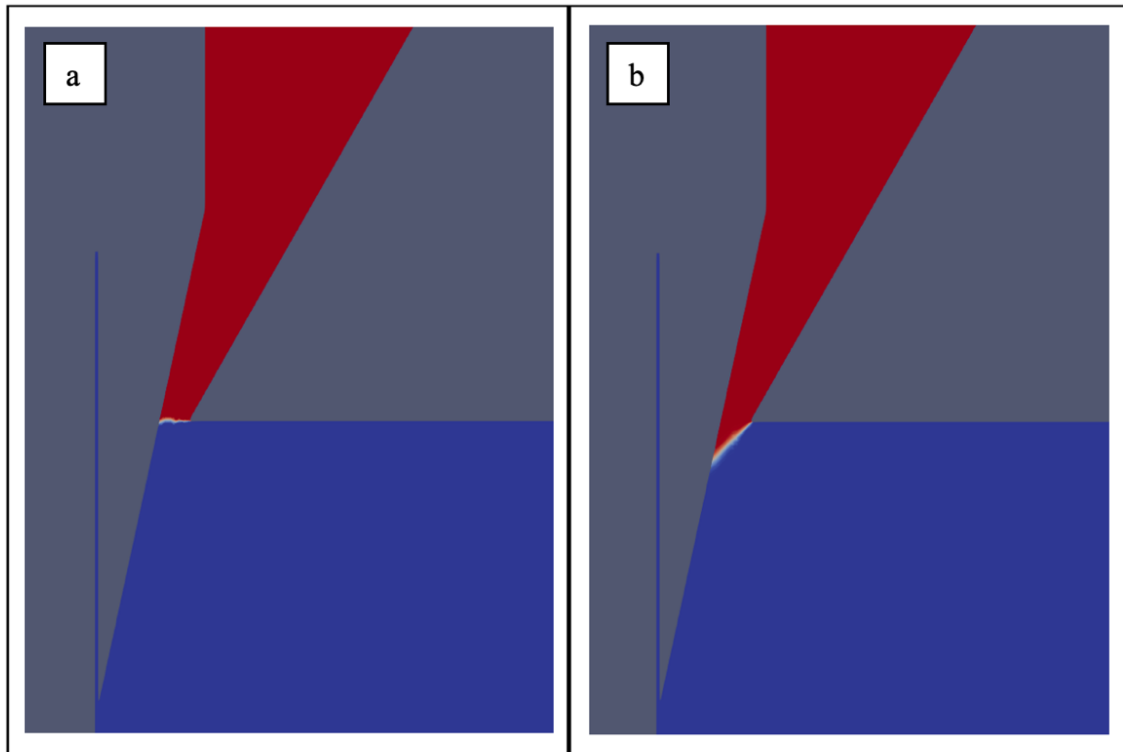


Fig.3.6: (a) Common initial shape of the bottom of the droplet for every simulation done; (b) Common final shape at the stationary of the bottom of the droplet for every simulation done.

Because of the required condition is not verified, it has been considered as degree of liberty the pin position against the orifice and further simulations have been done changing its position.

3.1.2 Simulations with $D_2 = 0.8 \text{ mm}$

In order to understand if a wider space between the orifice bottom diameter and the printing pin can satisfy the desired condition, several simulations have been done varying D_2 from 1.1 mm to 0.8 m (see Fig.2.3). In this, the only changed quantities are the contact angle with the pin and the radius of the droplet, while the contact angle with the orifice has been set at 60° .

On this way, the analysed cases are those of Fig.3.7.

Contact angle with the orifice	Radius of the droplet [m]	Contact angle with the pin
60°	[~1; 3; 4]	[5°; 30°; 60°]

Fig.3.7: Analysed values during the simulations.

Even in this case, the approach is the same. So, the initial positions used are those in which the droplet is positioned between orifice and pin space as shown in Fig.3.8.

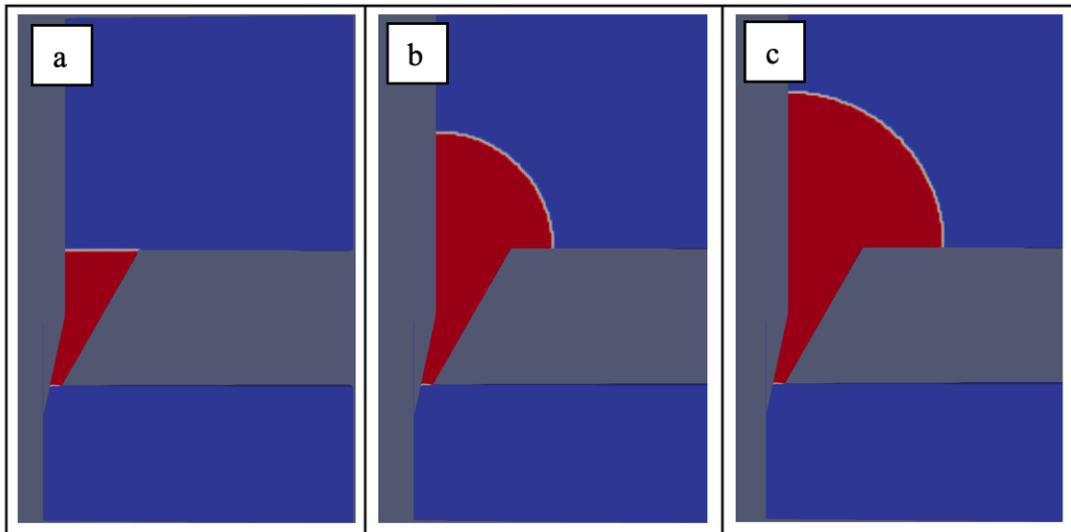


Fig.3.8: (a) Initial shape with $r \sim 1$ mm; (b) Initial shape with $r = 3$ mm; (c) Initial shape with $r = 4$ mm.

Varying the contact angle with the pin θ (Fig.3.9), the simulations have shown the following stationaries for the droplet with $r \sim 1$ mm.

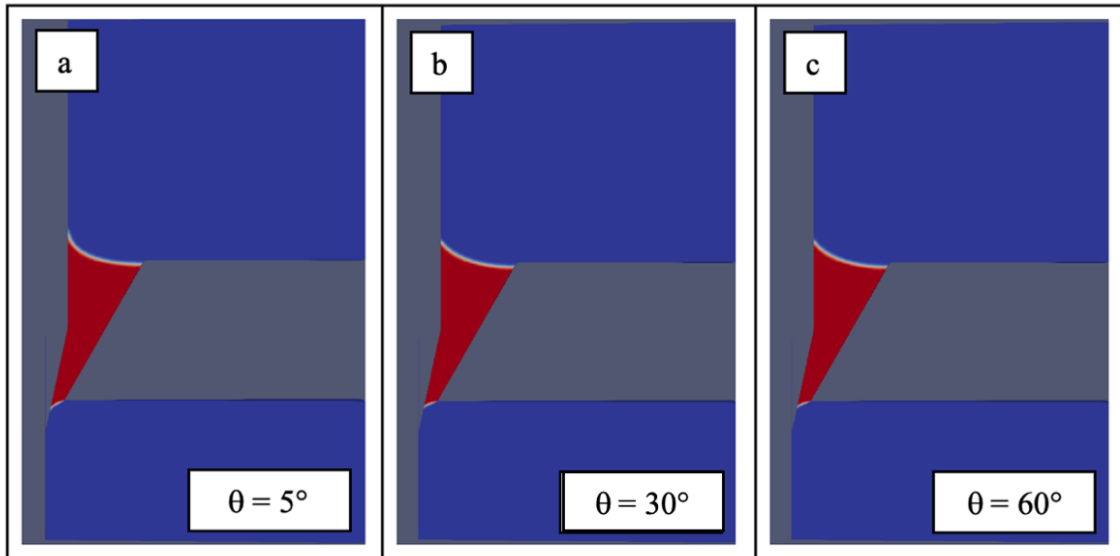


Fig.3.9: Simulations performed with a contact angle with the orifice of 60° , $r \sim 1$ mm and different contact angle with the pin. (a) Simulation with $\theta = 5^\circ$; (b) Simulation with $\theta = 30^\circ$; (c) Simulation with $\theta = 60^\circ$.

How can we see, the droplet is not able to pass.

Using a droplet with $r = 3$ mm, the same investigation has been performed. The simulations have shown the dynamics of Fig.3.10.

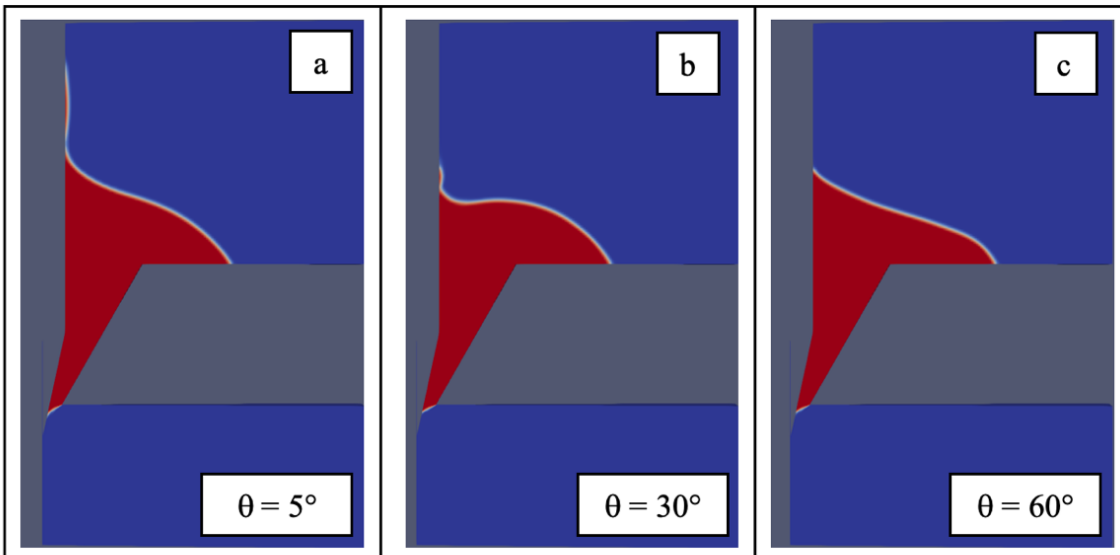


Fig.3.10: Simulations performed with a contact angle with the orifice of 60° , $r = 3$ mm and different contact angle with the pin. Every frame shows the situation at $t = 0.035$ s. (a) Simulation with $\theta = 5^\circ$; (b) Simulation with $\theta = 30^\circ$; (c) Simulation with $\theta = 60^\circ$

Although the dynamics are different before the stationary, the droplet is still not able to pass through the system.

At the end, the investigation has been made also for a droplet with $r = 4$ mm and the frames are in Fig.3.11.

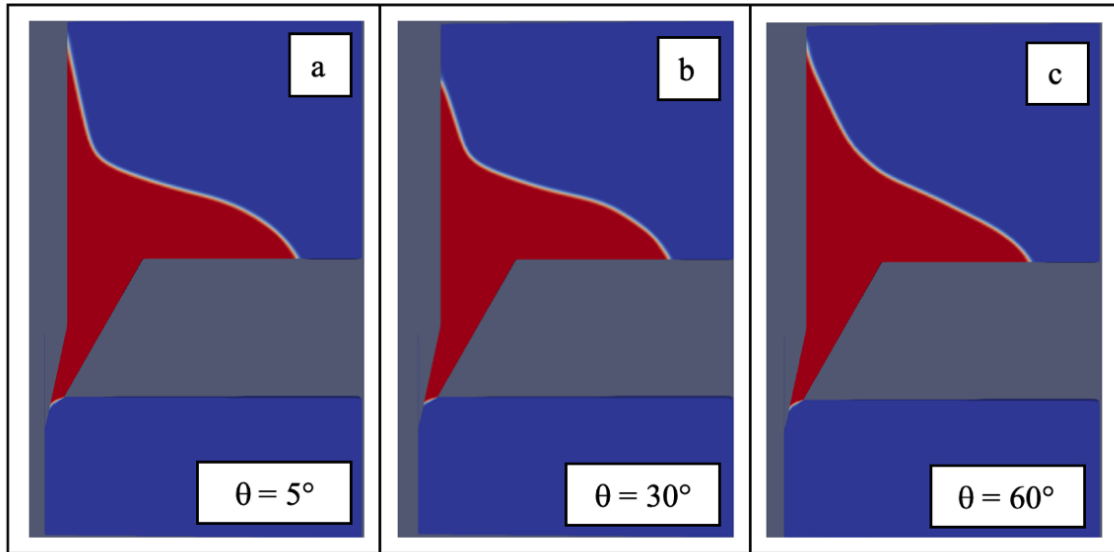


Fig.3.11: Simulations performed with a contact angle with the orifice of 60° , $r = 4$ mm and different contact angle with the pin. Every frame shows the situation at $t = 0.020$ s. (a) Simulation with $\theta = 5^\circ$; (b) Simulation with $\theta = 30^\circ$; (c) Simulation with $\theta = 60^\circ$.

Although the dynamics are different before the stationary, also in this case, the droplet is still not able to pass through the system.

Again, in every simulation done considering the parameters listed before, the droplet is not able to pass through the space between the orifice and the pin. Furthermore, the common stationary position of the bottom of the droplet for all analysed cases is specified in Fig.3.12.

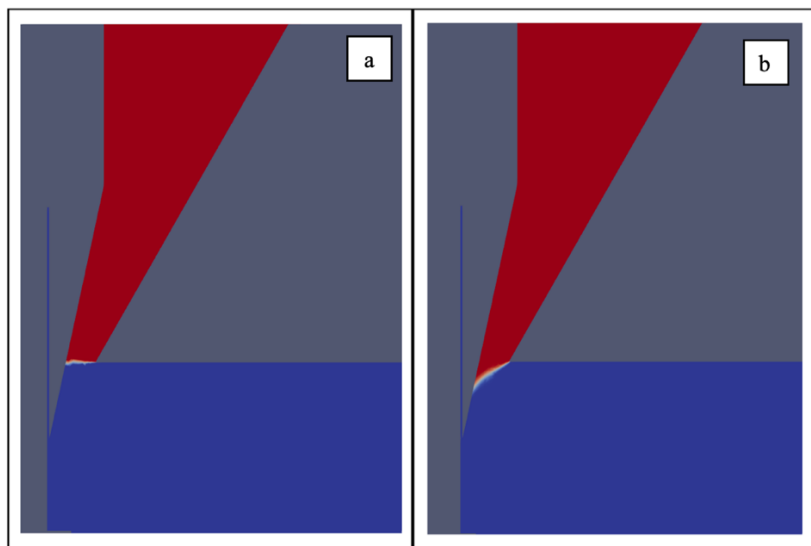


Fig.3.12: (a) Common initial shape of the bottom of the droplet for every simulation done; (b) Common final shape at the stationary of the bottom of the droplet for every simulation done.

3.1.3 Simulations with $D_2 = 0.5$ mm

To set another wider space between the orifice bottom diameter and the printing pin, several simulations have been done varying D_2 from 0.8 mm to 0.5 mm (see Fig.2.3). In this, the only changed quantities are the contact angle with the pin and the radius of the droplet, while the contact angle with the orifice has been set at 60° . On this way, the analysed cases are those of Fig.3.13.

Contact angle with the orifice	Radius of the droplet [m]	Contact angle with the pin
60°	[~1; 3; 4]	[5° ; 30° ; 60°]

Fig.3.13: Analysed values during the simulations.

The approach is always the same. So, the initial positions used are those in which the droplet is positioned between orifice and pin space as shown in Fig.3.14.

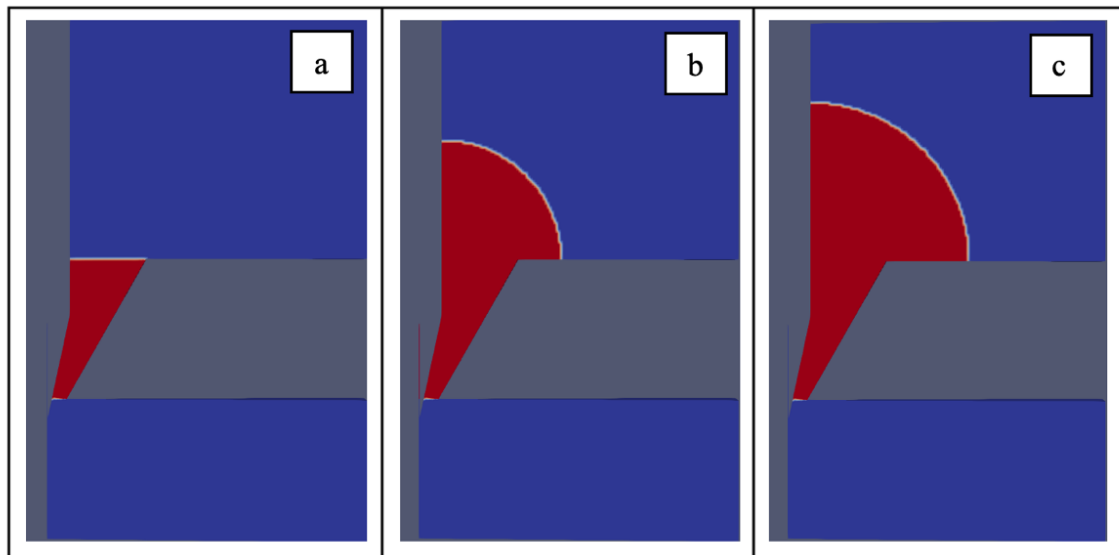


Fig.3.14: (a) Initial shape with $r \sim 1$ mm; (b) Initial shape with $r = 3$ mm; (c) Initial shape with $r = 4$ mm.

Varying the contact angle with the pin θ (Fig.3.15), the simulations have shown the following stationaries for the droplet with $r \sim 1$ mm.

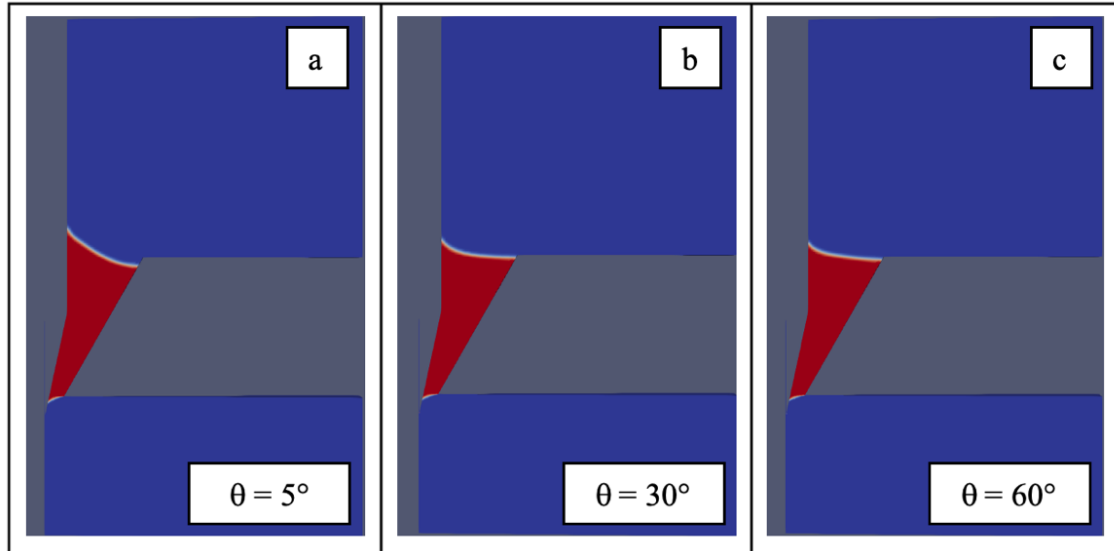


Fig.3.15: Simulations performed with a contact angle with the orifice of 60° , $r \sim 1$ mm and different contact angle with the pin. (a) Simulation with $\theta = 5^\circ$; (b) Simulation with $\theta = 30^\circ$; (c) Simulation with $\theta = 60^\circ$.

Even there, the droplet is not able to pass.

Using a droplet with $r = 3$ mm, the same investigation has been performed. The simulations have shown the dynamics of Fig.3.16.

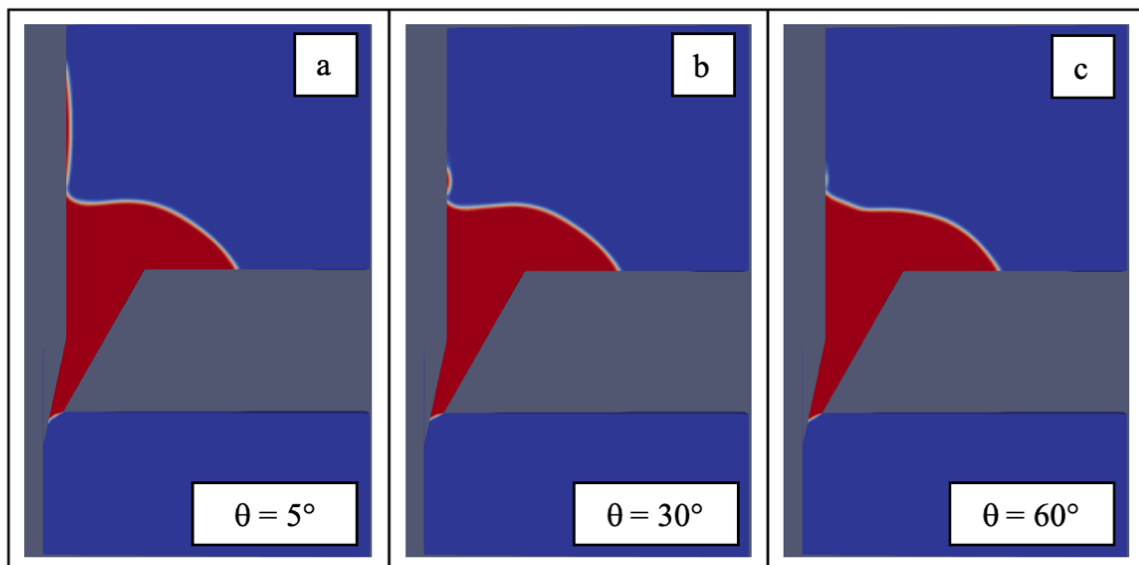


Fig.3.16: Simulations performed with a contact angle with the orifice of 60° , $r = 3$ mm and different contact angle with the pin. Every frame shows the situation at $t = 0.020$ s. (a) Simulation with $\theta = 5^\circ$; (b) Simulation with $\theta = 30^\circ$; (c) Simulation with $\theta = 60^\circ$.

Although the dynamics are different before the stationary, the droplet is still not able to pass through the system.

The investigation has been made also for a droplet with $r = 4$ mm and the frames are in Fig.3.17.

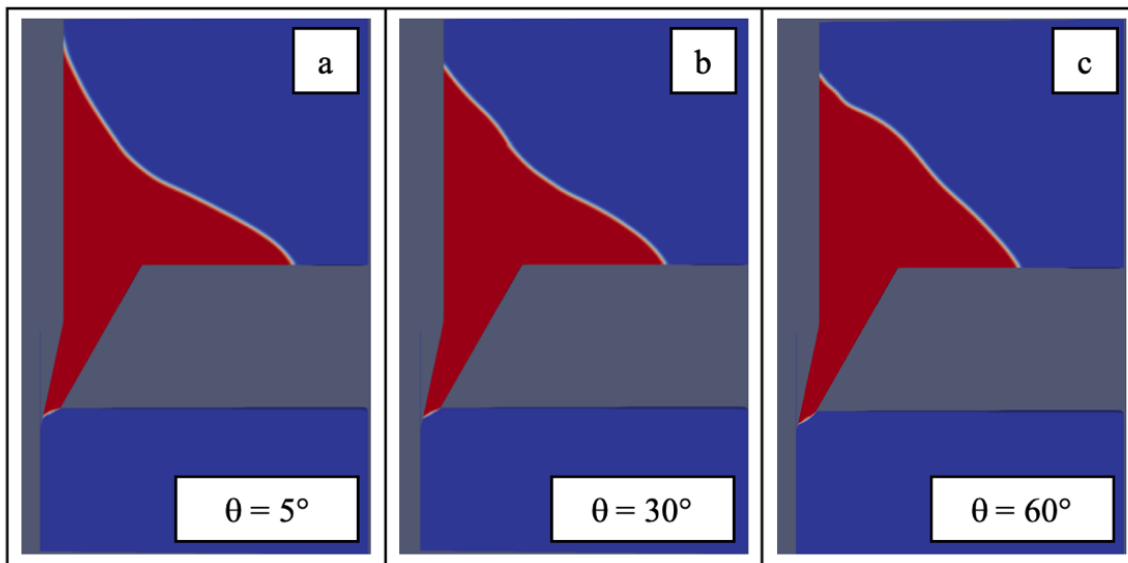


Fig.3.17: Simulations performed with a contact angle with the orifice of 60° , $r = 4$ mm and different contact angle with the pin. Every frame shows the situation at $t = 0.015$ s. (a) Simulation with $\theta = 5^\circ$; (b) Simulation with $\theta = 30^\circ$; (c) Simulation with $\theta = 60^\circ$.

Although the dynamics are not the same before the stationary, also in this case, the droplet is still not able to pass through the system.

So, also for $D_2 = 0.5$ mm, in every simulation done considering the parameters listed before, the droplet is not able to pass through the space between the orifice and the pin.

Furthermore, the common stationary position of the bottom of the droplet for all analysed cases is specified in Fig.3.18.

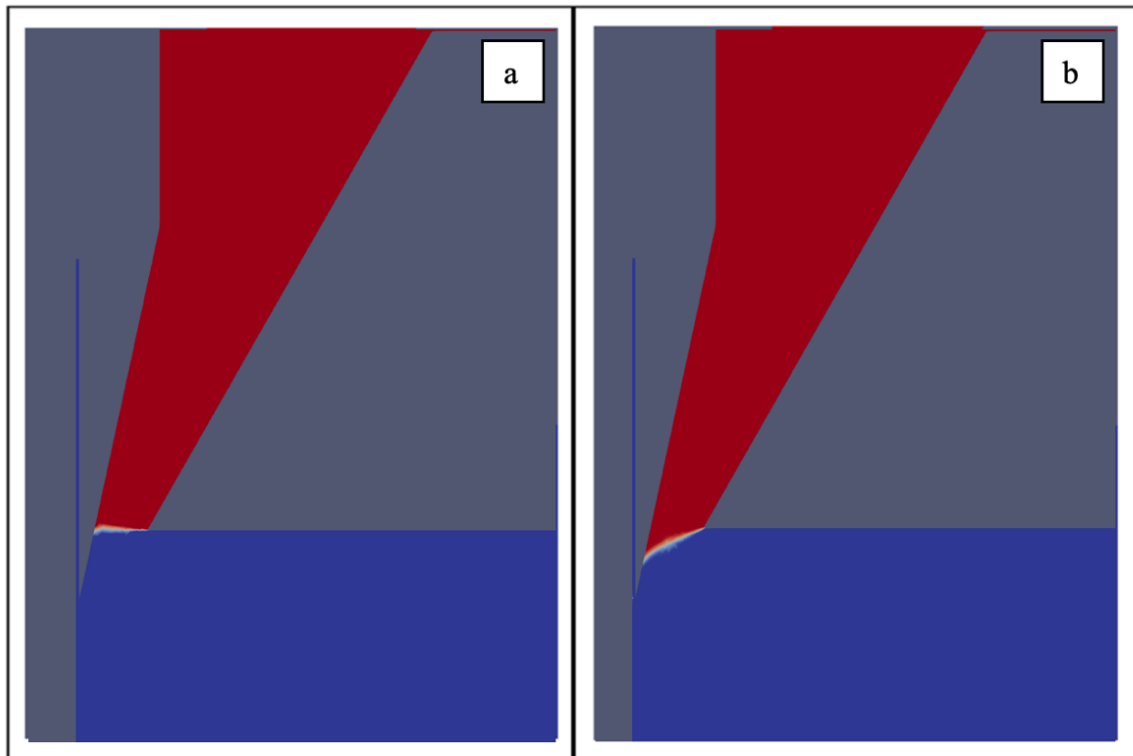


Fig.3.18: (a) Common initial shape of the bottom of the droplet for every simulation done; (b) Common final shape at the stationary of the bottom of the droplet for every simulation done.

Because of the required condition is not verified varying the position of the pin within the permitted limits too, we proceeded by modifying the physical properties of the material in order to understand in which range of them the shape of the meniscus is favoured. So, further simulations have been done.

3.2 Simulations of different fluids droplet through an orifice-pin system

Next simulations have been done to understand how the physical properties of the droplet changes the evolution of the dynamics. For this reason, no specific liquid has been used in them and the changing parameters used have been the contact angle with the pin θ , the contact angle with the orifice γ , the surface tension σ and the kinematic viscosity μ , while density ρ has been considered as a constant. All these simulations have been performed with standard CNR's geometry and assuming $r = 1.928 \text{ mm}$ (corresponding to $30\mu\text{l}$ in volume) as droplet radius. This choice has been made to have an experimental feedback, because, after the firsts simulation shown before, the CNR has begun to use a Gilson pipette with a sensibility of $30 \mu\text{l}$ to load the orifice-pin system. For the estimation of dimensionless numbers, the velocity has been set at 0.001 m/s as the common order of magnitude in the system and the characteristic length has been expressed as $l = r$.

The initial position used is common to all the next simulations and is that in which the droplet is positioned between orifice and pin space as shown in Fig.3.19. In this section we've used two different bottom shapes of the droplet in order to understand if a different initial configuration could change the dynamic.

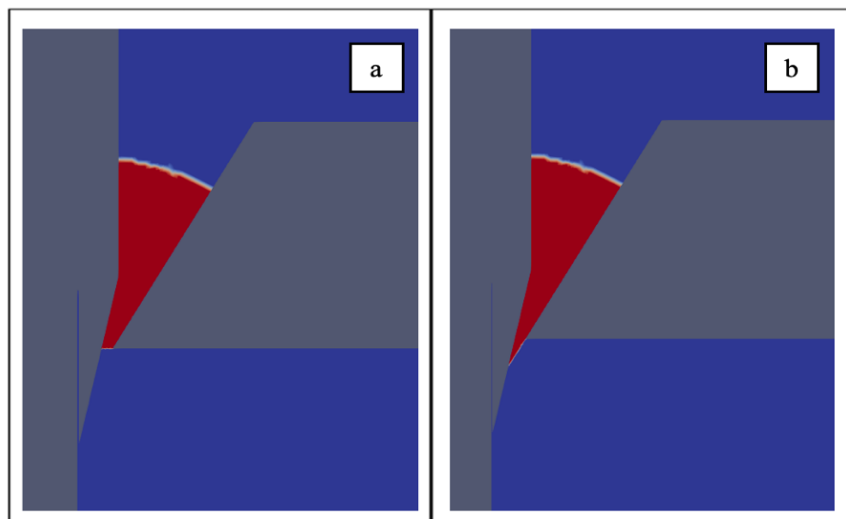


Fig.3.19: (a) Initial flat shape of the bottom of the droplet; (b) Initial elongated shape of the bottom of the droplet.

However, no change of dynamics has been highlighted and the initial shape condition of the bottom of the droplet will no longer be specified. In order to describe this kind of variations, the dimensionless numbers listed before have been used.

3.2.1 Simulations with variable Ca and Bo by variation of surface tension at fixed Re = 1.928

All the analysed cases in this section have been done considering kinematic viscosity and density as fixed parameters. In these, their values have been set to the distilled water one: $\mu = 1.00 \cdot 10^{-6} \text{ m}^2/\text{s}$ and $\rho = 1000 \text{ kg/m}^3$. So, the fixed value of the Re has been 1.928.

On this way, the analysed cases are those of Fig.3.20.

$\mu \text{ [m}^2/\text{s]}$	$\rho \text{ [kg/m}^3]$	$\sigma \text{ [N/m]}$	Contact angle with the orifice	Contact angle with the pin
$1.00 \cdot 10^{-6}$	1000	[0,0007; 0,00175; 0,0057; 0,0127; 0,0236; 0,010; 0,0175; 0,035; 0.105; 0.140]	[5°; 30°; 60°]	[5°; 30°; 60°]

Fig.3.20: Analysed values during the simulations.

The simulations have shown that the dynamics for $\sigma = 0.035 \text{ N/m}$ ($Bo = 1.042$; $Ca = 2.86 \cdot 10^{-5}$), $\sigma = 0.105 \text{ N/m}$ ($Bo = 0.347$; $Ca = 9.52 \cdot 10^{-6}$), $\sigma = 0.0236 \text{ N/m}$ ($Bo = 1.54$; $Ca = 4.23 \cdot 10^{-5}$), $\sigma = 0.0175 \text{ N/m}$ ($Bo = 2.08$; $Ca = 5.71 \cdot 10^{-5}$), and $\sigma = 0.140 \text{ N/m}$ ($Bo = 0.260$; $Ca = 7.14 \cdot 10^{-6}$), varying the contact angle with the orifice and the contact angle with the pin, are always the same. So, all the mentioned cases are shown one time in Fig.3.21.

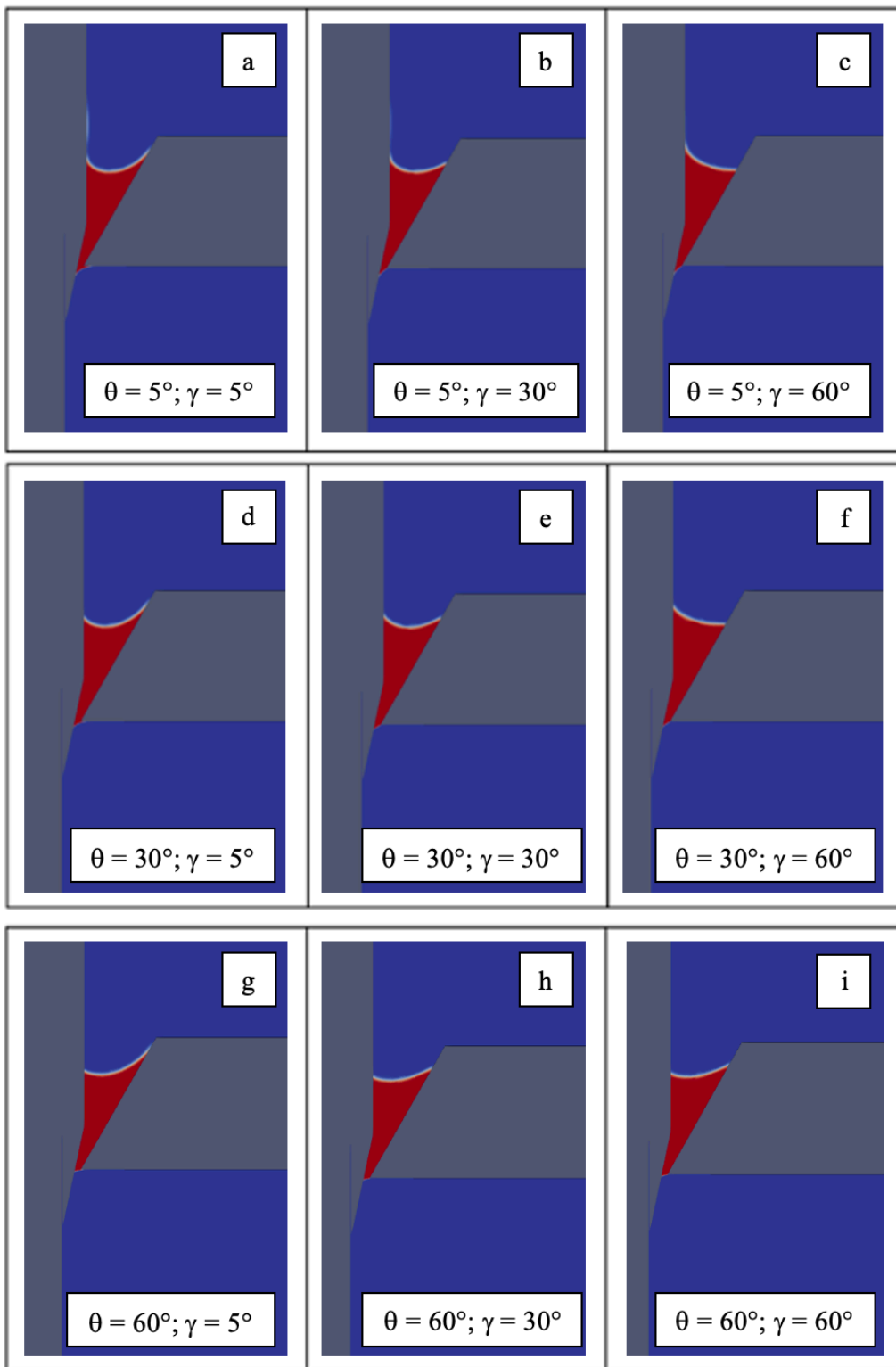


Fig.3.21: (a) Stationary with $\theta = 5^\circ$ and $\gamma = 5^\circ$; (b) Stationary with $\theta = 5^\circ$ and $\gamma = 30^\circ$; (c) Stationary with $\theta = 5^\circ$ and $\gamma = 60^\circ$; (d) Stationary with $\theta = 30^\circ$ and $\gamma = 5^\circ$; (e) Stationary with $\theta = 30^\circ$ and $\gamma = 30^\circ$; (f) Stationary with $\theta = 30^\circ$ and $\gamma = 60^\circ$; (g) Stationary with $\theta = 60^\circ$ and $\gamma = 5^\circ$; (h) Stationary with $\theta = 60^\circ$ and $\gamma = 30^\circ$; (i) Stationary with $\theta = 60^\circ$ and $\gamma = 60^\circ$.

How can we see, the droplet is never able to pass through the orifice-pin system, and the only change at the stationary is the way in which the droplet is placed between the pin and the orifice.

Instead, when $\sigma = 0.01$ ($Bo = 3.647$; $Ca = 0.0001$) the dynamic is different and is shown in Fig.3.22.

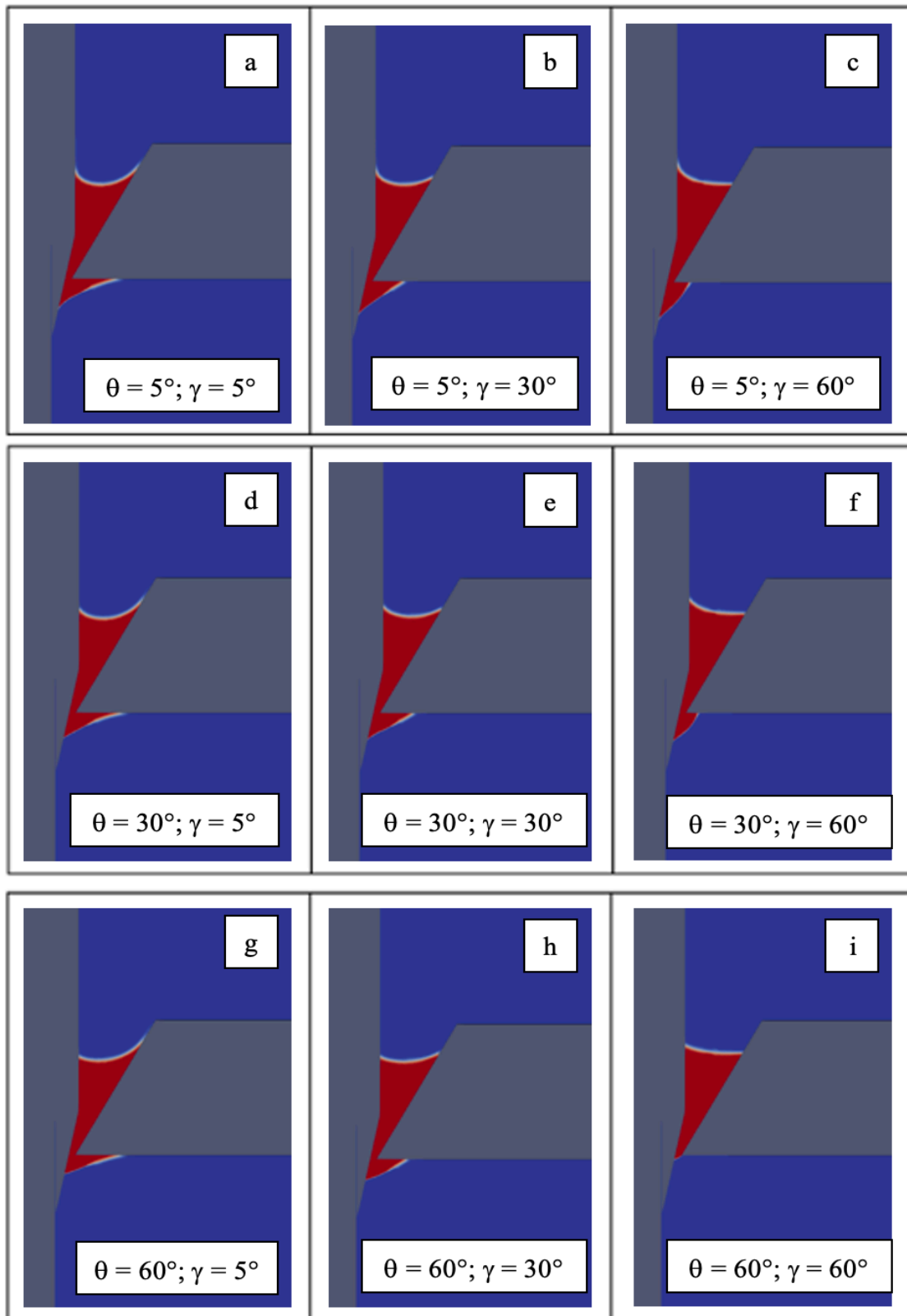


Fig.3.22: Dynamics at $t = 0.05s$ varying contact angles: (a) Dynamic with $\theta = 5^\circ$ and $\gamma = 5^\circ$; (b) Dynamic with $\theta = 5^\circ$ and $\gamma = 30^\circ$; (c) Dynamic with $\theta = 5^\circ$ and $\gamma = 60^\circ$; (d) Dynamic with $\theta = 30^\circ$ and $\gamma = 5^\circ$; (e) Dynamic with $\theta = 30^\circ$ and $\gamma = 30^\circ$; (f) Dynamic with $\theta = 30^\circ$ and $\gamma = 60^\circ$; (g) Dynamic with $\theta = 60^\circ$ and $\gamma = 5^\circ$; (h) Dynamic with $\theta = 60^\circ$ and $\gamma = 30^\circ$; (i) Dynamic with $\theta = 60^\circ$ and $\gamma = 60^\circ$.

Fig.3.22 reports a frame of the dynamics at general time ($t = 0.05s$) in order to highlight the difference between the cases in the most objective way possible. In it, it's clear that the droplet is able to pass in all condition except that with $\theta = 60^\circ$ and $\gamma = 60^\circ$; moreover, the way in which the droplet is placed on the bottom of the plate and the pin shows how a different contact angles with the walls can influence the shape of the droplet and consequently the dynamic. This influence is expressed also in term of rate of fall during all dynamics (Fig.3.23 and Fig.3.24) and it's even more evident in the last case with $\theta = 60^\circ$ and $\gamma = 60^\circ$ in which the droplet stops before passing on the system.

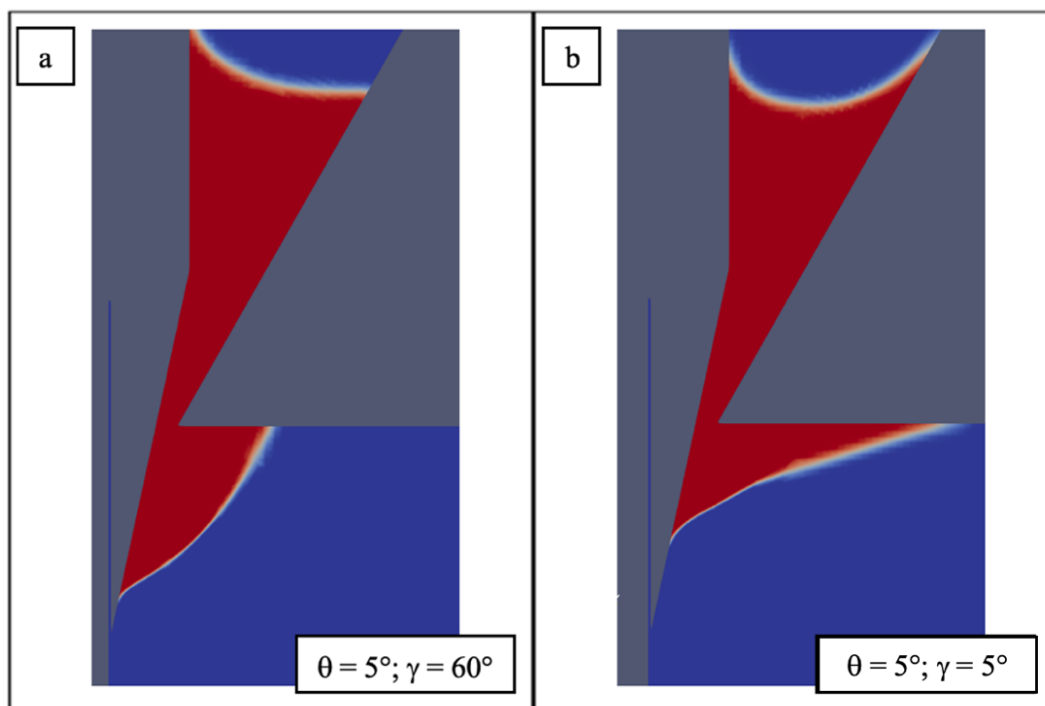


Fig.3.23: Dynamics at $t = 0.1s$ varying contact angles: (a) Dynamic with $\theta = 5^\circ$ and $\gamma = 60^\circ$; (b) Dynamic with $\theta = 5^\circ$ and $\gamma = 5^\circ$.

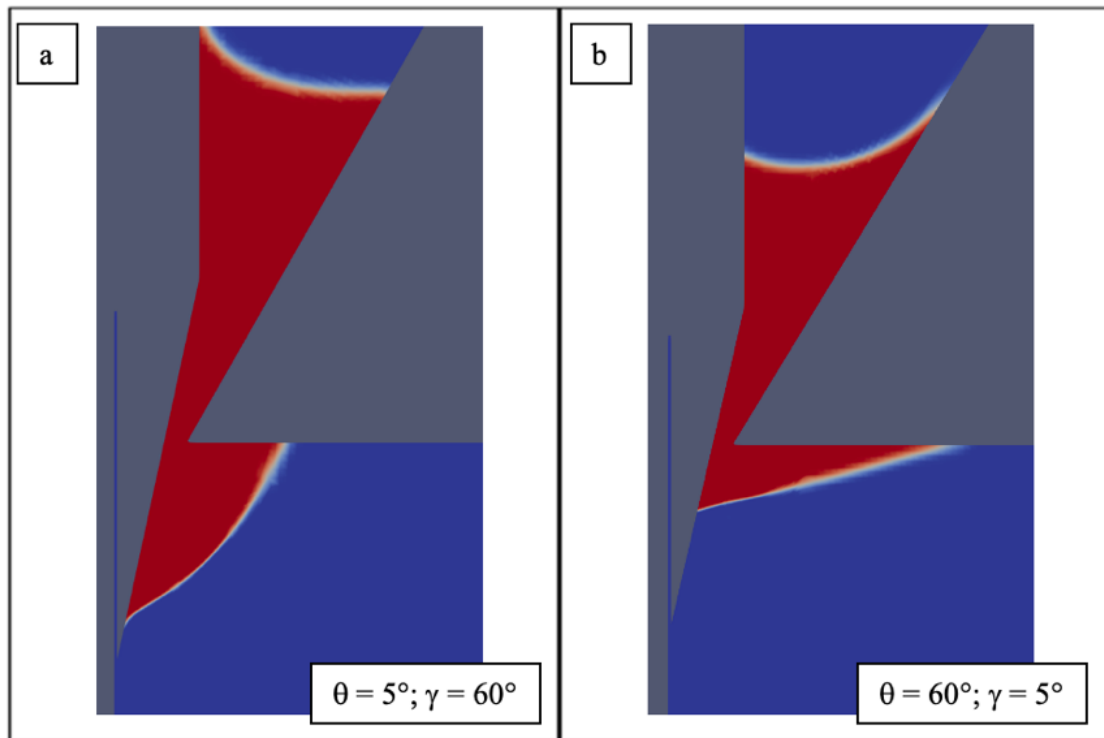


Fig.3.24: Dynamics at $t = 0.05$ varying contact angles: (a) Dynamic with $\theta = 5^\circ$ and $\gamma = 60^\circ$; (b) Dynamic with $\theta = 60^\circ$ and $\gamma = 5^\circ$.

From the frames, it's clear that low contact angles with the pin and high contact angles with the orifice favour the flow of the droplet.

However, for other cases as $\sigma = 0.00571$ N/m ($Bo = 6.38$; $Ca = 0.000175$), $\sigma = 0.0007$ N/m ($Bo = 52.09$; $Ca = 0.0014$), $\sigma = 0.00175$ N/m ($Bo = 20.84$; $Ca = 0.00057$) and $\sigma = 0.0127$ N/m ($Bo = 2.87$; $Ca = 7.87 \cdot 10^{-5}$), the dynamic is similar to the one expressed in Fig.3.22 (the droplet is able to go through the system), but the interaction of the contact angles in the flow is different. In particular, higher Bo favour the flow also for $\theta = 60^\circ$ and $\gamma = 60^\circ$.

In order to summarize, it can be affirmed that liquids with same density and kinematic viscosity of the distilled water (corresponding to $Re = 1.928$) and surface tension greater than a factor 1.5 and 2 and lower than factor 2 compared to the one of distilled water, are not able to satisfy the first required condition (the flow between pin and orifice) while

liquids with surface tension lower than a factor 7 yes. The dynamic is the more favourable the more the difference of the contact angles is wider. It can be explained, referring to a higher Bond number Bo (see 1.3.1 in Chapter 1) than the one of the distilled water (case in which the droplet is not able to go through). In this term, the gravity force beats the surface tension force and this interaction make possible the flow.

However, the factor 7 is not the transition factor between flow and no flow conditions. In fact, other simulations have been made in order to understand for $Bo = n \cdot Bo^{H_2O}$ what is the n -factor of transition considering the contact angles used too. The results for $Re = 1.928$ are shown in Fig.3.25.

$\theta \searrow \begin{matrix} \rightarrow \\ \gamma \end{matrix}$	5°	30°	60°
5°	4 (red) 5 (green)	4 (red) 5 (green)	6 (red) 6.50 (green)
30°	4 (red) 5 (green)	4 (red) 5 (green)	6.50 (red) 7 (green)
60°	4 (red) 5 (green)	5 (red) 6 (green)	8 (red) 9 (green)

Fig.3.25: Transition factors with $\mu = 1.00 \cdot 10^{-6} \text{ m}^2/\text{s}$ varying the contact angles. In red the last n -factor in which there is no flow, while in green the first n -factor in which the droplet flows.

So, the corresponding Bo values are:

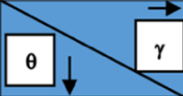
	5°	30°	60°
5°	2.08375 (red) 2.6046 (green)	2.08375 (red) 2.6046 (green)	2.6046 (red) 3.3860 (green)
30°	2.08375 (red) 2.6046 (green)	2.08375 (red) 2.6046 (green)	3.3860 (red) 3.6465 (green)
60°	2.08375 (red) 2.6046 (green)	2.6046 (red) 3.1256 (green)	4.16749 (red) 4.6884 (green)

Fig.3.26: Transition Bo values varying the contact angles. In red the last value in which the is no flow, while in green the first value in which the droplet flows.

3.2.2 Simulations with variable Ca and Re by variation of kinematic viscosity at fixed Bo = 0.5209

To analyse the variations of Ca and Re, we've carried out some simulations with variable kinematic viscosity. All the analysed cases in this section have been done considering density and surface tension as a fixed parameter. In these, their values have been set to the distilled water one: $\rho = 1000 \text{ kg/m}^3$ and $\sigma = 0.07 \text{ N/m}$ (Fig.3.27). The corresponding Bond Number is $Bo = 0.5209$.

$\mu \text{ [m}^2\text{/s]}$	$\rho \text{ [kg/m}^3]$	$\sigma \text{ [N/m]}$	Contact angle with the orifice	Contact angle with the pin
[$7.00 \cdot 10^{-6}$; $1.00 \cdot 10^{-7}$; $1.00 \cdot 10^{-8}$]	1000	0.07	[5°; 30°; 60°]	[5°; 30°; 60°]

Fig.3.27: Analysed values during the simulations.

The simulations have shown that the dynamics for $\mu = 7.00 \cdot 10^{-6} \text{ m}^2/\text{s}$. ($\text{Re} = 0.275$; $\text{Ca} = 0.0001$), $\mu = 1.00 \cdot 10^{-7} \text{ m}^2/\text{s}$ ($\text{Re} = 19.28$; $\text{Ca} = 1.42 \cdot 10^{-6}$) and $\mu = 1.00 \cdot 10^{-8} \text{ m}^2/\text{s}$ ($\text{Re} = 192.8$; $\text{Ca} = 1.42 \cdot 10^{-7}$) varying the contact angle with the orifice and the contact angle with the pin, are always the same: the droplet is never able to pass through the orifice-pin system, and the only change at the stationary is the way in which the droplet is placed between the pin and the orifice. The dynamics are the same of those in Fig.3.21.

Other values of kinematic viscosity haven't been analysed because a split of another 10-factor of them brings the dynamics in the turbulent regime that is an unreal case of study.

3.2.3 Other Simulations varying Bo, Re and Ca simultaneously

Other simulations have been performed in order to understand the dynamics of the droplet through an orifice-pin system varying Bo, Re and Ca simultaneously. In these, the only constant value considered has been the density $\rho = 1000 \text{ kg/m}^3$, while surface tension and kinematic viscosity values have been simultaneously changed (Fig.3.28). In all cases, $\theta = 5^\circ$ and $\gamma = 60^\circ$.

Re	Ca	Bo	Desired condition
0.275	$2.00 \cdot 10^{-4}$	1.04	no
19.28	$2.85 \cdot 10^{-6}$	1.04	no
192.8	$2.85 \cdot 10^{-7}$	1.04	no
0.275	$3.70 \cdot 10^{-4}$	1.92	no
19.28	$5.28 \cdot 10^{-6}$	1.92	no
192.8	$5.28 \cdot 10^{-7}$	1.92	no
0.964	$1.10 \cdot 10^{-4}$	2.08	no
0.964	$2.00 \cdot 10^{-4}$	3.64	yes
0.964	$3.50 \cdot 10^{-4}$	6.38	yes
0.964	$2.80 \cdot 10^{-3}$	52.09	yes
3.50	$3.14 \cdot 10^{-5}$	2.08	yes
3.50	$5.50 \cdot 10^{-5}$	3.64	yes
3.50	$9.62 \cdot 10^{-5}$	6.38	yes
3.50	$7.80 \cdot 10^{-4}$	52.09	yes
0.275	$7.00 \cdot 10^{-4}$	3.64	yes
0.275	$1.20 \cdot 10^{-3}$	6.38	yes
0.275	$1.00 \cdot 10^{-2}$	52.09	yes
19.28	$1.00 \cdot 10^{-5}$	3.64	yes
19.28	$1.75 \cdot 10^{-5}$	6.38	yes

19.28	$1.40 \cdot 10^{-4}$	52.09	yes
192.8	$1.00 \cdot 10^{-6}$	3.64	yes
192.8	$1.75 \cdot 10^{-6}$	6.38	yes
192.8	$1.40 \cdot 10^{-5}$	52.09	yes
0.107	$1.00 \cdot 10^{-3}$	2.08	no
0.107	$1.80 \cdot 10^{-3}$	3.64	yes
0.107	$3.10 \cdot 10^{-3}$	6.38	yes
0.107	$2.60 \cdot 10^{-2}$	52.09	yes
0.107	$1.00 \cdot 10^{-2}$	20.83	yes
964	$1.14 \cdot 10^{-7}$	2.08	yes
964	$2.00 \cdot 10^{-7}$	3.64	yes
964	$3.50 \cdot 10^{-7}$	6.38	yes
964	$2.86 \cdot 10^{-6}$	52.09	yes
964	$1.14 \cdot 10^{-6}$	20.83	yes
0.964	$1.10 \cdot 10^{-3}$	20.83	yes
3.50	$3.10 \cdot 10^{-4}$	20.83	yes
19.28	$5.71 \cdot 10^{-5}$	20.83	yes
192.8	$5.71 \cdot 10^{-6}$	20.83	yes
0.275	$4.00 \cdot 10^{-3}$	20.83	yes

964	$1.57 \cdot 10^{-6}$	2.87	yes
0.107	$1.40 \cdot 10^{-3}$	2.87	no
0.964	$1.57 \cdot 10^{-4}$	2.87	no
3.50	$4.33 \cdot 10^{-5}$	2.87	yes
19.28	$7.87 \cdot 10^{-6}$	2.87	yes
192.8	$7.87 \cdot 10^{-7}$	2.87	yes
0.275	$5.50 \cdot 10^{-4}$	2.87	no
964	$5.71 \cdot 10^{-8}$	1.04	yes

Fig.3.28: Analysed dimensionless numbers during the simulations.

Their corresponding results are shown in Fig.3.29.

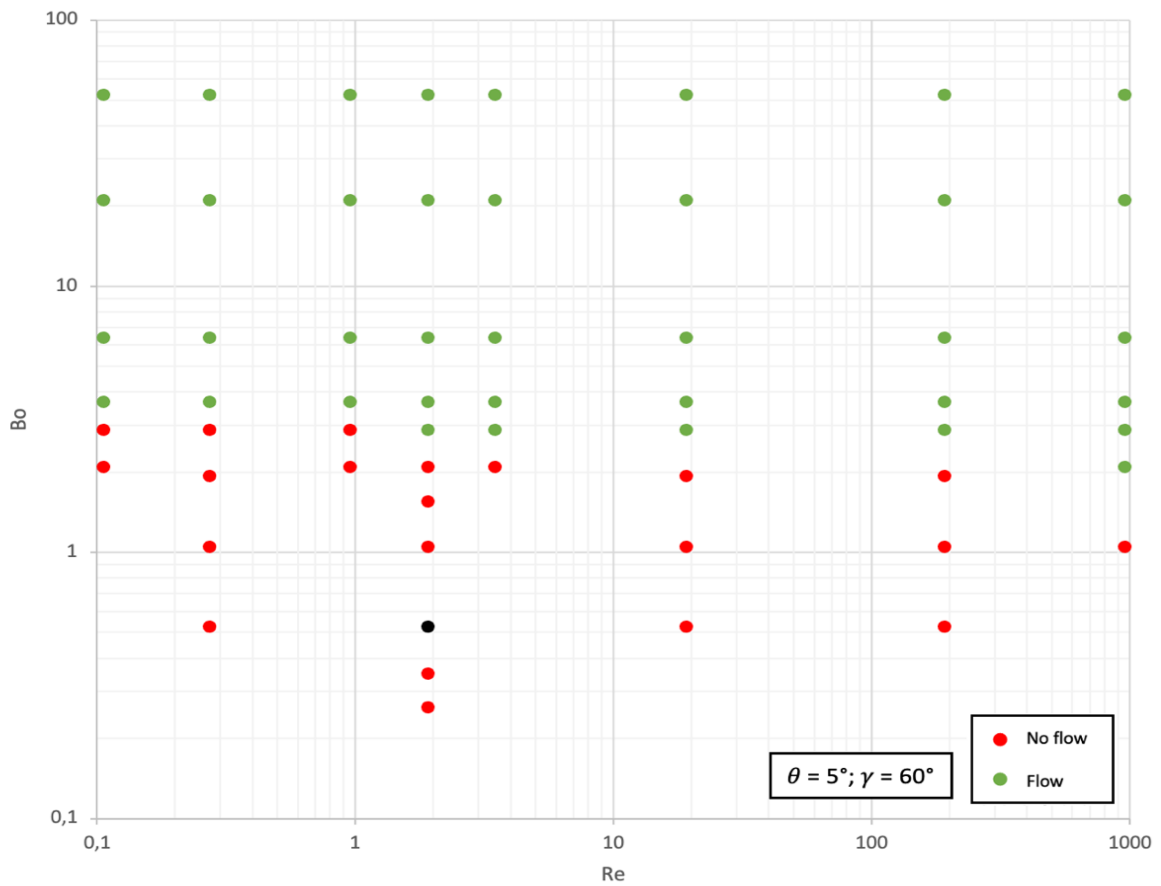


Fig.3.29: Results of simulations with variable Bo, Re and Ca with $\theta = 5^\circ$ and $\gamma = 60^\circ$. In black, the standard case of distilled water.

3.3 Meniscus formation and complete dynamic

Once we've analysed the conditions in which the droplet is able to go through the system, it remains to be verified that a meniscus shape is formed. The computational time for these simulations is critically higher, for this reason only the conditions in which the flow of the droplet is favoured have been firstly analysed. In particular, a higher n-factor for Bo improves the rate of dynamics although the shape of the flow always remains the same, so it has been considered n-factor = 100.

So, the first analysed case is the one in which $\theta = 5^\circ$, $\gamma = 60^\circ$, $\sigma = 0.0007$ N/m, $\rho = 1000$ kg/m³ and $\mu = 1 \cdot 10^{-6}$ m²/s with $Re = 1.928$, $Ca = 1.42 \cdot 10^{-3}$ and $Bo = 52.09$. Here, the decrease of 100 of surface tension is balanced with a decrease of 100 in the characteristic length, so the $Bo = Bo_{NO\ FLOW}^{H_2O}$ of the initial case in which the droplet of distilled water wasn't able to go through the orifice-pin system. On this way, it's reasonable thinking that the droplet, after passing through the space between orifice and pin, gets stuck on the tip of the pin and forms the desired meniscus.

Meniscus formation during the last part of the flow is described in Fig.3.30

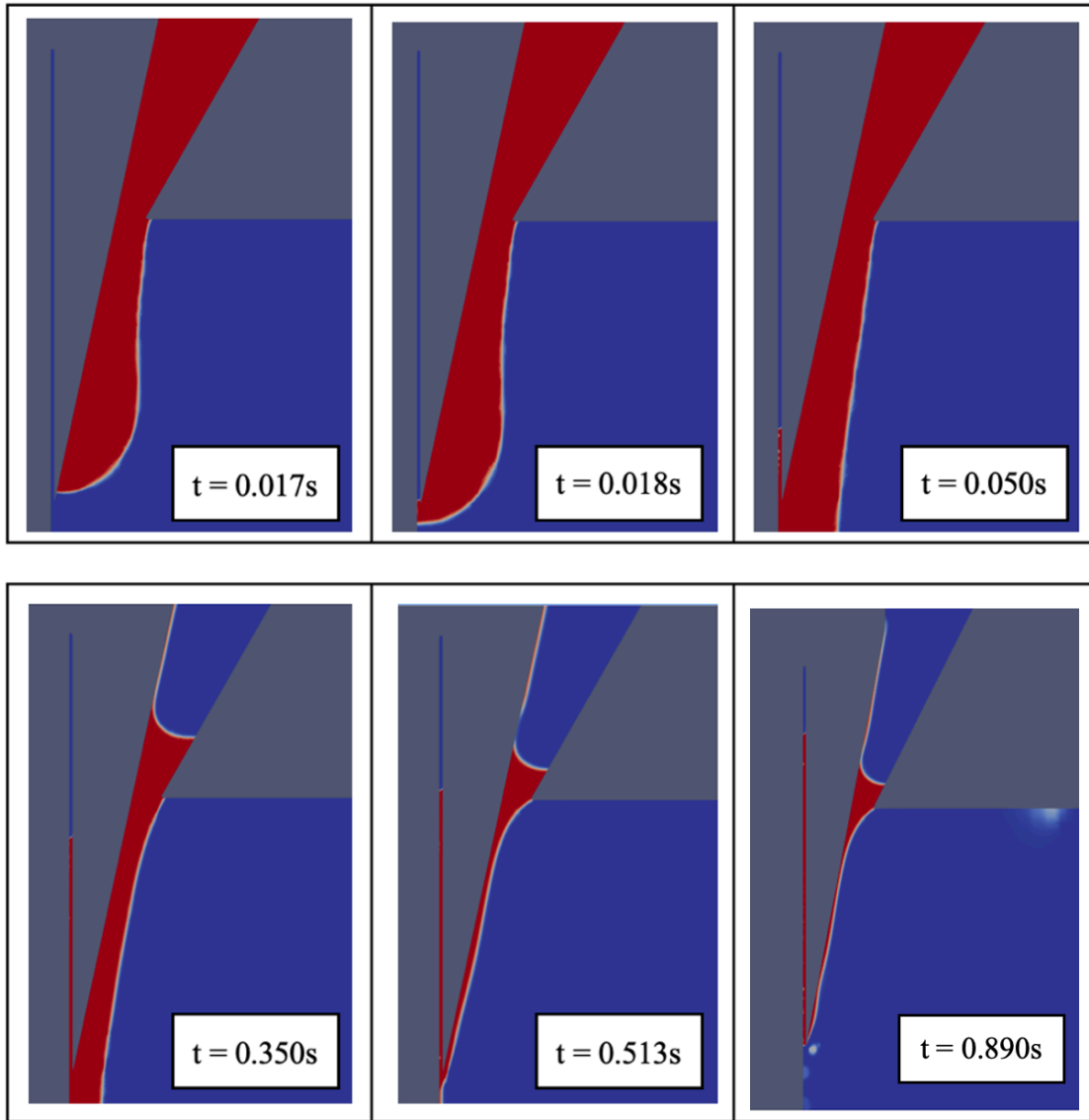


Fig.3.30: Evolution of the dynamic of meniscus formation.

While a recap of the complete dynamic is shown in Fig.3.31.

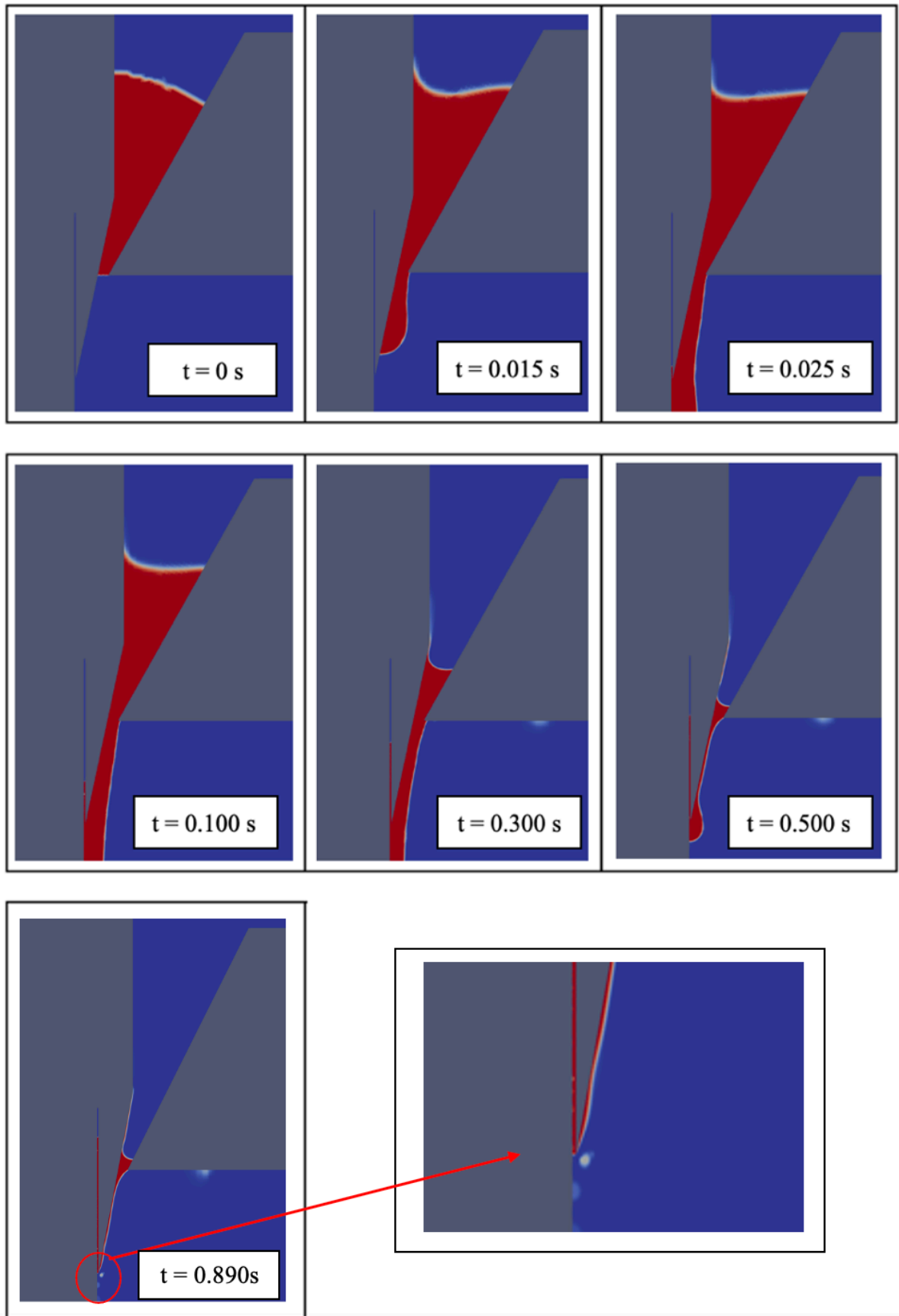


Fig.3.31: Evolution of the dynamic of the droplet.

However, for other contact angles, the final meniscus shape is similar to that shown before, but higher contact angles with the pin seems to create a no-film condition on the wall of the pin. Other cases are in Fig3.32.

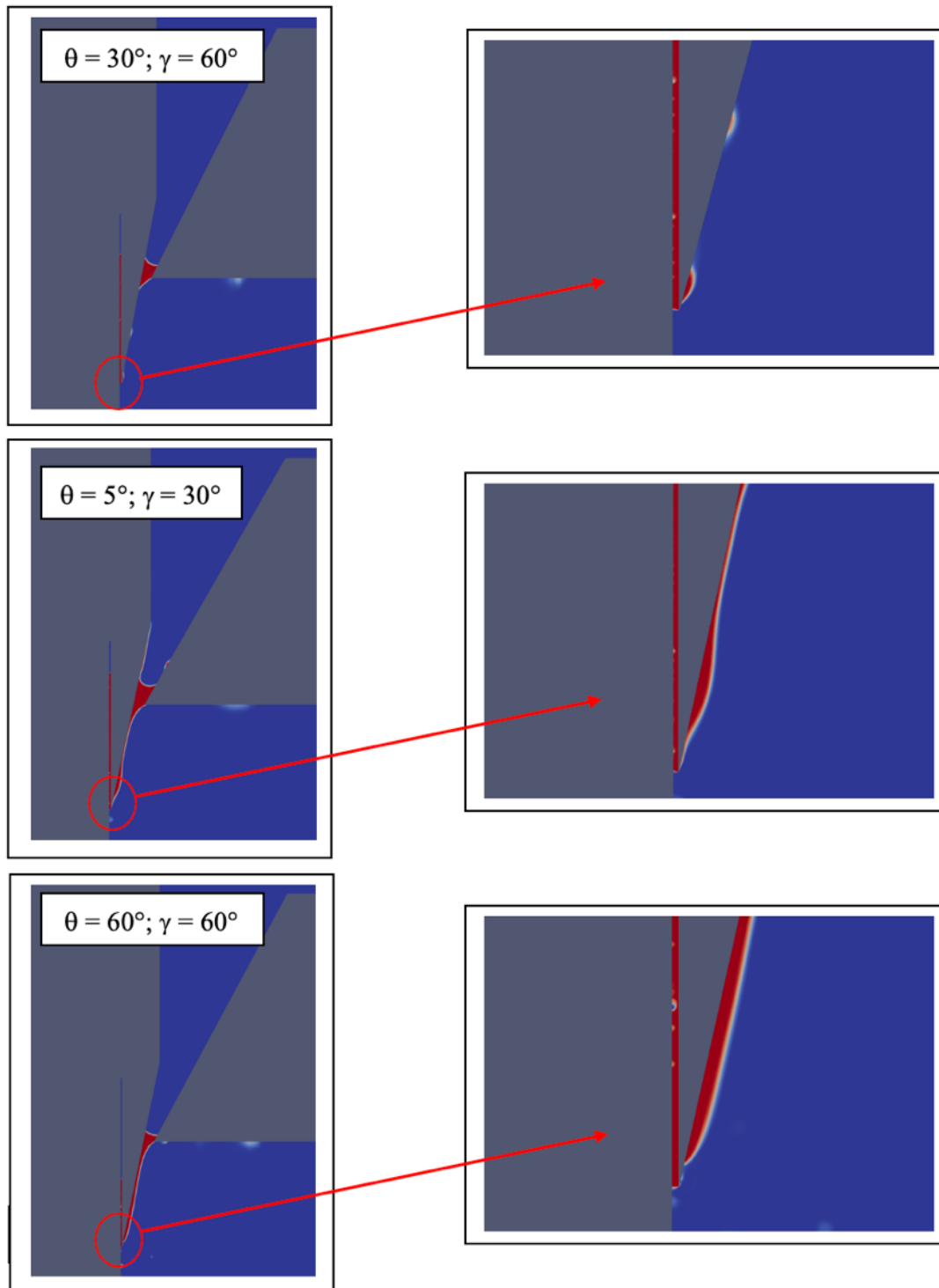


Fig.3.32: (a) Final meniscus shape for $\theta = 30^\circ$ and $\gamma = 60^\circ$;(b) Final meniscus shape for $\theta = 5^\circ$ and $\gamma = 30^\circ$; (c) Final meniscus shape for $\theta = 60^\circ$ and $\gamma = 60^\circ$.

3.4 Effect of initial velocity

Although the results of the simulations have been satisfactory, it remains to remember that some assumptions were made. In fact, all the cases have been studied considering a 2D axisymmetric geometry and the initial velocity of the liquid as zero. The effect of geometry simplification will be understood with experimental tests by CNR-ISASI, while the effect of initial velocity can be analyzed with other simulations. For this reason a simulation with $U_0 = 20$ cm/s, $Re = 1.928$, $Bo = 1.8$, $\theta = 5^\circ$ and $\gamma = 60^\circ$ is shown in Fig.3.33.

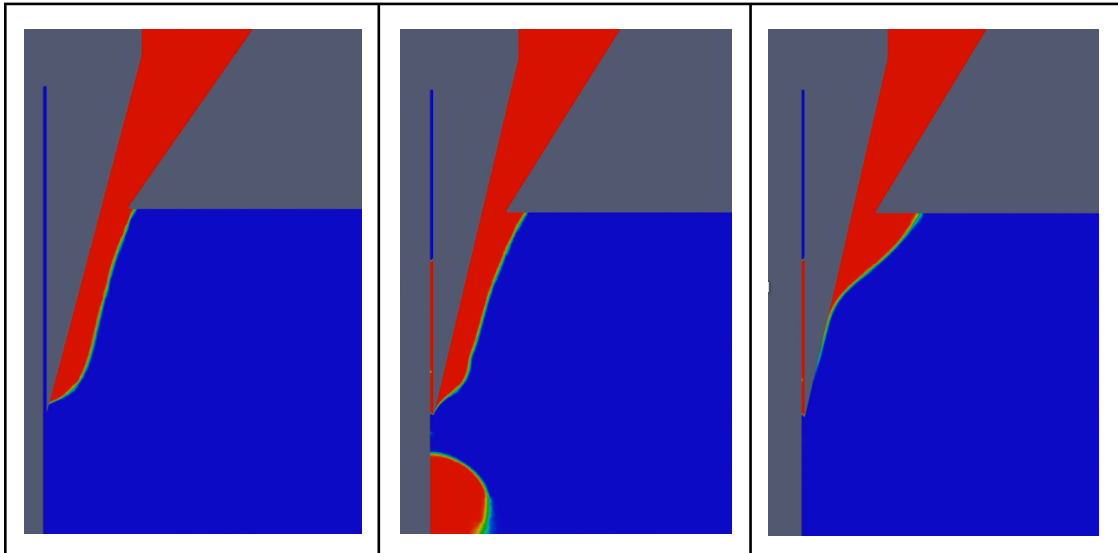


Fig.3.33: Evolution of dynamic for $U_0 = 20$ cm/s, $Re = 1.928$, $Bo = 1.8$, $\theta = 5^\circ$ and $\gamma = 60^\circ$.

The droplet initially flows, models the meniscus and returns back while a meniscus is formed.

Other simulations, instead, have been made considering the physical parameters of the water, so the corresponding analyzed values have been $Re = 1.928$, $Bo = 0.5209$, $\theta = 5^\circ$ and $\gamma = 60^\circ$, while the initial velocity has been set first to the value of $U_0 = 20$ cm/s (Fig.3.34) and then to the value of $U_0 = 30$ cm/s (Fig.3.35).

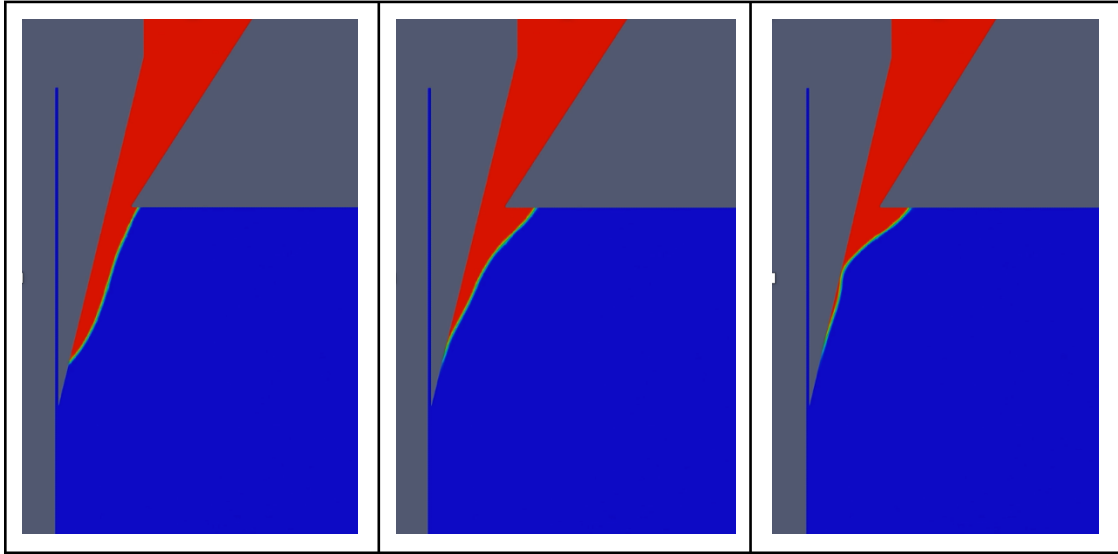


Fig.3.34: Evolution of dynamic for $U_0 = 20$ cm/s, $Re = 1.928$, $Bo = 0.5209$, $\theta = 5^\circ$ and $\gamma = 60^\circ$.

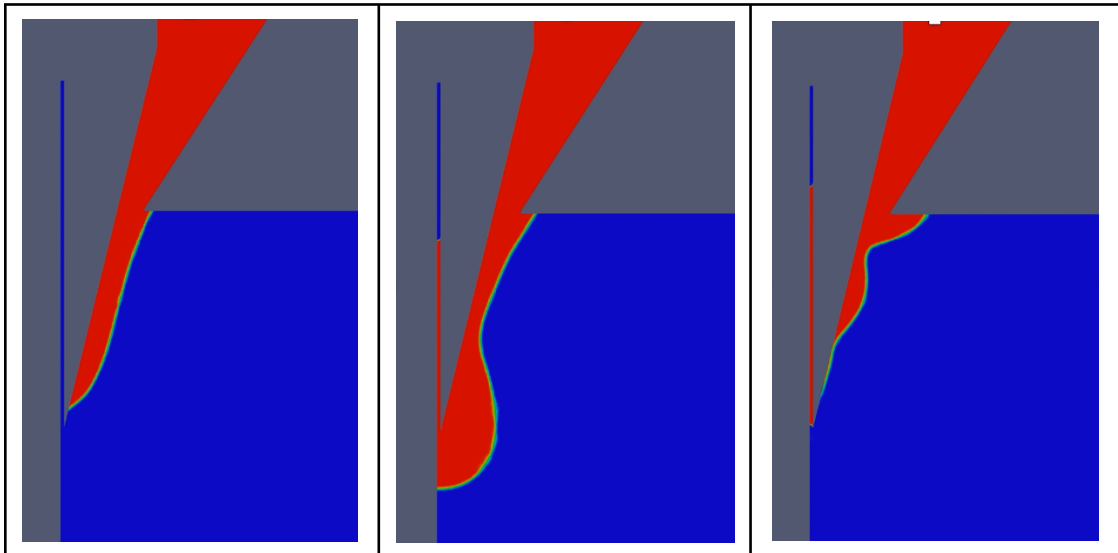


Fig.3.35: Evolution of dynamic for $U_0 = 30$ cm/s, $Re = 1.928$, $Bo = 0.5209$, $\theta = 5^\circ$ and $\gamma = 60^\circ$.

Even if it could be a different initial velocity in experimental tests, it's evident that it will exercise a positive effect on the meniscus formation.

CHAPTER 4

CONCLUSIONS

In this thesis, numerical simulations of droplet dynamics through an orifice-pin system for pyro-electrodynamic shooting were made. In order to pursue that, a VOF method-based code is used.

The aim of this work is to report the results of simulations in which were varied the contact angles with the walls: at first, varying the characteristic length, and after the physical properties of the liquid.

The desired condition is that in which the droplet goes through the orifice-pin system and creates a meniscus shape on the tip of the printing pin.

For SensApp set up, a shift of the pin in a higher position is not able to make possible the flow, so physical properties have been analyzed in order to understand in which conditions a generic droplet flows without changing the current components (the pin and the plate with the orifice). Some dimensionless numbers describe the problem: Ca, Bo and Re.

Referring to the distilled water values for this system ($Re = 1.928$; $Bo = 0.5209$ and $Ca = 1.42 \cdot 10^{-5}$), the simulations have shown that higher Bo and Re favour the dynamics. Compared to distilled water values, some transition multiplicative n-factor for the Bo have been expressed, all between 5 and 9. While, there is no transition multiplicative n-factor for Re due to the laminar flow limit. The more multiplicative factors are higher, the more the droplet flows through the system faster. A specific table for these transition values of Bo has been reported in the work too. However, the n-factor of transition change by varying the contact angles with the walls.

In fact, the contact angles with the pin and orifice influence the way the droplets flow. Even when the n-factor is near to the n-factor of transition,

the combination $\theta = 60^\circ$ and $\gamma = 60^\circ$ stops the droplet and became a critical parameter for the dynamic. Considering the rate of fall, the droplet flows through the orifice-pin system in a favoured way when the contact angles with the pin are low and the contact angles with the orifice are high, however, for the meniscus formation, higher contact angles with the pin shows a no-film condition on the wall of the pin.

In order to confirm these evidence, experimental tests will be carried out by the CNR-ISASI in next months. Even if it could be a different initial velocity in these tests, it will exercise a positive effect on the meniscus formation.

These results may help a lot of people on the early diagnosis of Alzheimer's disease in order to improve the quality of their life through preventive treatments, but this approach could also be extended to the diagnosis of other diseases and to numerous biomedical applications in order to make better living conditions.

Further studies may be carried out analyzing different values of contact angles in the meniscus formation and analyzing if the same results could be obtained with cheaper components (different radius of the orifice, different kind of pin) in order to make the devices as cheap as possible.

BIBLIOGRAPHY

1. Clark, M. F., Lister, R. M. & Bar-Joseph, M. ELISA techniques. in *Methods in Enzymology* vol. 118 742-766 (Academic Press, 1986).
2. SensApp. *SensApp* <http://www.sensapp.eu/>.
3. Whitesides, G. The origins and the future of microfluidics. *Nature* **442**, 368-373 (2006)
4. Konda A, Morin SA (June 2017). "Flow-directed synthesis of spatially variant arrays of branched zinc oxide mesostructures". *Nanoscale*. 9 (24): 8393-8400.
5. Chokkalingam V, Tel J, Wimmers F, Liu X, Semenov S, Thiele J, et al. (December 2013). "Probing cellular heterogeneity in cytokine-secreting immune cells using droplet-based microfluidics". *Lab on a Chip*. **13**(24): 4740-4
6. Le Pesant et al., Electrodes for a device operating by electrically controlled fluid displacement, U.S. Pat. No. 4,569,575, Feb. 11, 1986.
7. Liu M, Suo S, Wu J, Gan Y, Ah Hanaor D, Chen CQ (March 2019). "Tailoring porous media for controllable capillary flow". *Journal of Colloid and Interface Science*. **539**: 379-387.
8. Munaz A, Shiddiky MJ, Nguyen NT (May 2018). "Recent advances and current challenges in magnetophoresis based micro magnetofluidics". *Biomicrofluidics*. **12** (3): 031501.
9. Wang, H., Chen, L. & Sun, L. Digital microfluidics: A promising technique for biochemical applications. *Front. Mech. Eng.* **12**, 510-525 (2017).

10. Wheeler A R. Putting electrowetting to work. *Science*, 2008, 322 (5901): 539-540
11. A. Casner, J.-P. Delville, *Phys. Rev. Lett.* 90, 144503 (2003)
12. R.T. Collins et al., *Nat. Phys.* 4, 149-154 (2008)
13. Coppola S. (2016) Pyro-Electrohydrodynamic Printing and Multi Jets Dispenser. In: *Manipulation of Multiphase Materials for Touch-less Nanobiotechnology*. Springer Theses (Recognizing Outstanding Ph.D. Research). Springer, Cham.
14. Maeda, N., Israelachvili, J. N. & Kohonen, M. M. Evaporation and instabilities of microscopic capillary bridges. *Proc. Natl Acad. Sci. USA* 100, 803-808 (2003).
15. Ferraro, P., Coppola, S., Grilli, S. *et al.* Dispensing nano-pico droplets and liquid patterning by pyroelectrodynamic shooting. *Nature Nanotech* 5, 429-435 [2010].
16. Faraone A, Master Thesis: Dispensing pico droplets by pyroelectrohydrodynamic jetting: simulations and experimental results, 21-22 [2019]
17. <https://openfoam.org>